Pure Appl. Geophys.

https://doi.org/10.1007/s00024-024-03638-2

Pure and Applied Geophysics

Peculiar Variations and Long-term Changes in Sea Level Observed in the Lanzarote Geosciences Laboratory (Canary Islands, Spain)

M. Benavent,[1,5] J. Arnoso,[2,5] E. J. Vélez,[2,5] F. G. Montesinos,[1,5] U. Tammaro,[3] and U. Riccardi[4,5]

Abstract—We use tide gauge data spanning from 2005 to 2023 in the Geosciences Laboratory at Lanzarote (Canary Islands, Spain) to perform a detailed analysis of the local short and long-term changes not previously examined in this area. Sea level is affected by the spatial and temporal climate variability on annual to decadal time scales. Consequently, the analysis of the linear trends of sea level can be difficult even when long time series are available. To achieve this objective, we investigate multi-year (from 3 to 10 years) and decadal variations of sea level through its connection with climate indexes such as the sea surface temperature, the sunspots or the North Atlantic Oscillation (NAO). First, we apply the standard corrections for the ocean tides, the atmospheric dynamics and the interannual and seasonal variability of the observed time series. Second, we study the sea level changes at multi-year to decadal scales by applying the maximal overlap discrete wavelet transform for the decomposition of the sea level signal. Furthermore, the correlations between the sea level and complementary data (sea water temperature, sunspot number and NAO Index) are investigated by means of the cross-wavelet and wavelet coherence methods. Finally, we perform a linear regression analysis of the sea level changes with the sea water temperature, including periodic components, to model the observed sea level data. Jointly with the tide gauge data, the sea level is monitored using a GNSS permanent station co-located with the tide gauge site. The study of both time series (sea level and vertical ground displacement), after removal of the previously modelled tidal and non-tidal components, provides the long-term linear trend for the complete period, from 2005 to 2023: an increase of 0.33 ± 0.06 cm/yr for the sea level and an increase of about 0.016 ± 0.003 cm/yr for GNSS-vertical displacement.

Keywords: Sea level, ground deformation, tidal and non-tidal components, multi-resolution analysis, wavelet coherence, Canary Islands.

1. Introduction

Regional sea level changes can be quite different from the global mean owing to different oceanic, atmospheric and climatic conditions (Marrero-Betancort et al., 2022). The regional variability of the sea level is the result of a sum of processes working on different space (up to thousands of kilometres) and time scales (from hours to decades). Some of the processes can be well determined as they occur periodically at well-known frequencies, such as the ocean tides. Other intermediate and long-term sea-level changes are influenced by temperature or atmospheric pressure variations (among others), that induce non-periodic signals of varying amplitude and duration. Therefore, it becomes necessary to investigate the possible correlations between sea level and meteorological forcing and climate indices at different time scales. Furthermore, sea level and climate indices can be affected by the solar variability at a wide range of time scales. In particular, the 11 year Schwabe (or sunspot) cycle, is present in the sea surface temperature (SST) but its response is not uniform (Yamakawa et al., 2016).

Thus, to estimate long-term trends in series containing considerably non-stationary interannual and decadal variability it is appropriate to analyse sea level records using time–frequency methods (Erol, 2011; Li, 2008).

Supplementary Information The online version contains supplementary material available at https://doi.org/10.1007/s00024-024-03638-2.

[1] Facultad de CC. Matemáticas, Universidad Complutense de Madrid, Plaza de Ciencias 3, 28040 Madrid, Spain.

[2] Instituto de Geociencias (IGEO, CSIC-UCM), C/Doctor Severo Ochoa, 7, 28040 Madrid, Spain. E-mail: jose.arnoso@csic.es

[3] Istituto Nazionale Di Geofisica E Vulcanologia, Napoli, Italy.

[4] Università "Federico II" Di Napoli, Napoli, Italy.

[5] Research Group 'Geodesia' (GRG-UCM), Universidad Complutense de Madrid, 28040 Madrid, Spain.

Published online: 07 January 2025

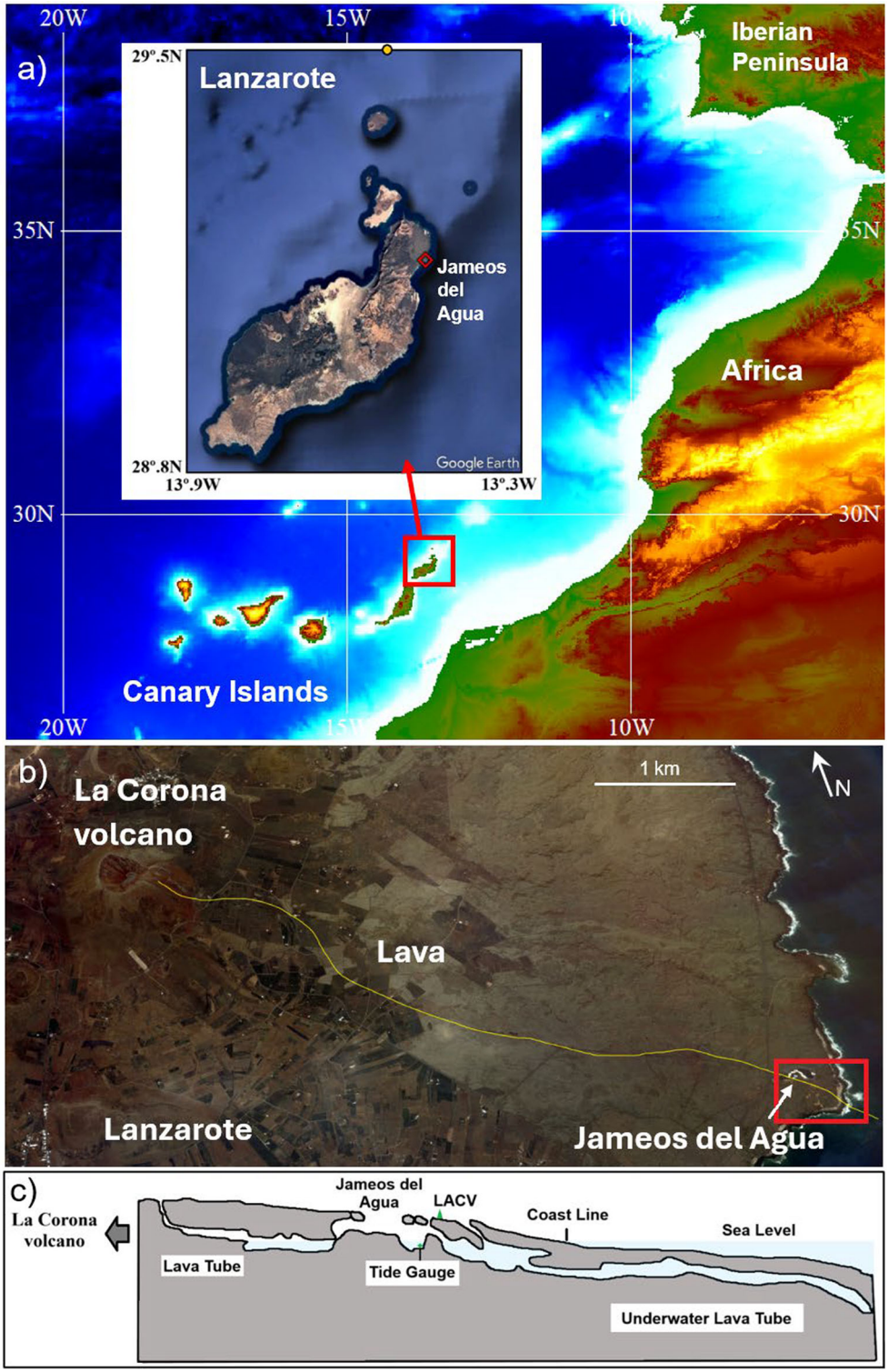

Surface deformations measured in the vicinity of the coast can be indicative of changes in the observed sea level. Indeed, land subsidence can accelerate sea level rise in coastal regions, and results in socio-

◀Figure. 1
a Location of Lanzarote Island in the Canary archipelago (Spain). The inset shows the location of Jameos del Agua (JA) site at the northeast of the island. The bathymetry is taken from GEBCO database. **b** Google Earth image showing the location of JA site in the lava tube (yellow line) of the La Corona volcano, within the facilities of the Geosciences Laboratory of Lanzarote. The orange circle points the centre of the grid cell with SST data. **c** Profile view of the final part of the lava tube (red square in b) showing the location of the tide gauge and GNSS station (LACV) at JA site (modified from Martínez-García et al., 2016)

economic consequences. GNSS (Global Navigation Satellite System) stations are widely used to monitor surface deformations, and if co-located in the vicinity of tide gauge sites can detect vertical land motion that can be removed from the relative variation of the sea level to provide an absolute estimate of the sea level change in the study area (Hwang et al., 2016; Wöppelmann & Marcos, 2016). In active volcanic areas near to the coastline, sea level observations can also be carried out to assess vertical movements of the ground linked to volcanic signals. In fact, apparent changes in sea level can be produced by ground uplift or subsidence associated with volcano dynamics. In this context, sea level control acts as an important indicator for volcano monitoring systems (Berrino et al., 1998; Corrado et al., 1981; Tammaro et al., 2021).

In this paper, we investigate the use of the multi resolution analysis based in the maximal overlap discrete wavelet (MRA-MODWT) to identify components that could be susceptible to be subtracted from the sea level time series (if we are able to relate them with a meteorological o climatic context) to allow a better assessment of the sea level change.

Grinsted et al. (2004) showed how cross-wavelet transform and the wavelet coherence methods can be applied to non-stationary geophysical time series to deal with localized intermittent periodicities by estimating the correlation of the time series in the time–frequency domain. Song et al. (2023) used wavelet coherence and partial wavelet coherence to establish a relationship between monthly mean sea level and up to 15 climate indexes on various time scales (influencing factors such as CO_2 concentration, sea ice area, and sunspots) in different regions of the world, including the north Atlantic Ocean. Also, Kirikkaleli and Sowah (2021) employ wavelet analysis to investigate links between global average temperature anomalies and global sea level.

In the Canary Islands, the tidal regime is predominately semidiurnal, with amplitudes ranging from 0.58 to 0.84 m for the dominant M2 constituent, which increases from south to north (Gómez et al., 2015). The Canary Islands, at a latitude near 28° N, lie on the coastal transitional zone between the northwest African upwelling region and the open ocean waters of the subtropical gyre (see, for instance Fig. 1 in Siemer et al., 2021 and Fig. 1b in Marrero-Betancort et al., 2022); this is the so called "Canary Current". In this area climate patterns as the North Atlantic Oscillation (NAO) have impacts on the ocean dynamics at scales of interannual to decadal variability, resulting in non-stationary sea level changes and trends (Zhu et al., 2023). García-Lafuente et al. (2004) investigated the contribution of different components to the annual cycle of the sea level at different harbours of the Canary Islands. They observed that the annual cycles are aligned with the SST ones, but amplitudes differ from one island to another, which is interpreted as the local response to large-scale seasonal changes of the Canary Current. Marrero-Betancort et al. (2022) also studied correlations between sea level observations and the SST in the Canary region focussing on seasonal intra-annual and annual components.

In this work, we applied various analysis methods to the sea level time series from the tide gauge located in Jameos del Agua (JA) site (ϕ = 29°.16 N, λ = 13°.43 W), to the northeast of Lanzarote, Canary Islands archipelago (Fig. 1a). The tide gauge is installed in a lake that results from the intersection of the lava tube of La Corona volcano with the ocean (Fig. 1b; 1c). The lava tube emerges from the volcano, spans 6 km until it reaches the coastline and enters the ocean for approximately 1.8 km. The only direct connection between the lava tube and the ocean is a small hole situated at 750 m offshore the coastline. The indirect connection between them occurs through cracks, fissures and the porosity of the volcanic rocks (Martinez García et al., 2016). The instruments located in this lake form part of the Geosciences Laboratory of Lanzarote, which is

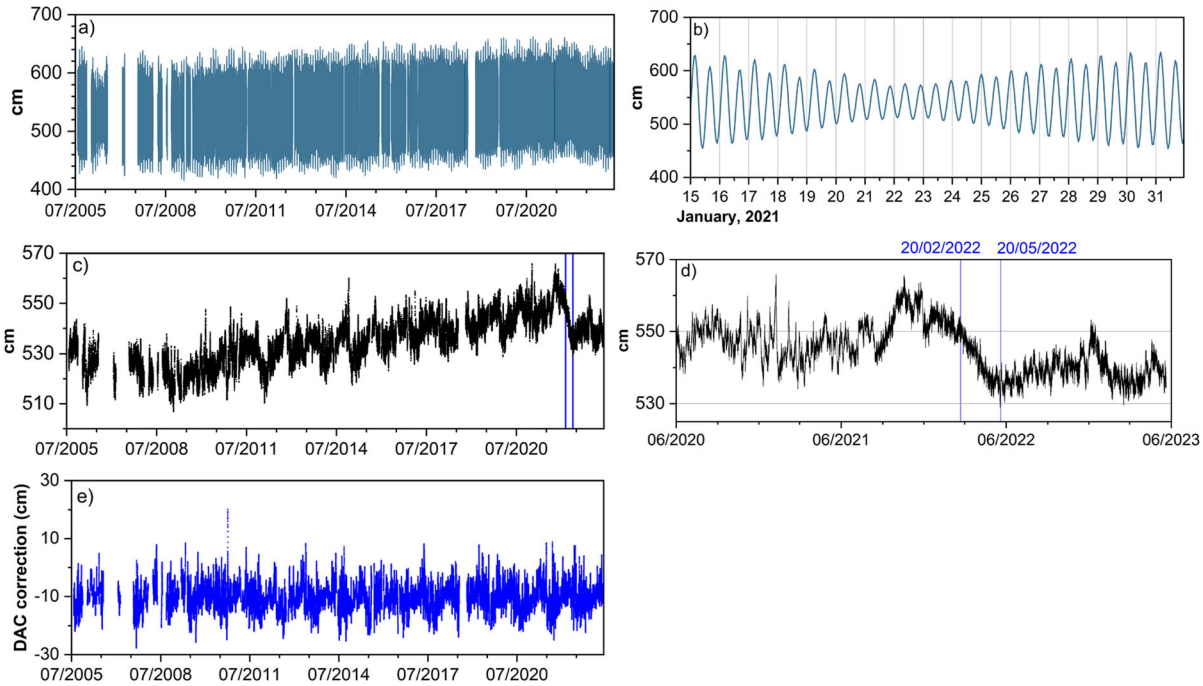

Figure. 2
a Observed sea level at JA site (Lanzarote), for the period 2005–2023. **b** Extended range for 2021 year showing the observed tides. **c** The observed sea level of a) after tidal removal. The blue lines indicate the period from February 20 to May 20, 2022. **d** Zoom over the last three years of c). **e** Dynamic atmospheric correction (DAC) applied to the observed sea level data

devoted to investigate the geodynamic activity in Lanzarote Island and to promote geodetic and geophysical researches to study active areas of the Earth. Monitoring of sea level is one of the research objectives of the laboratory (Arnoso et al., 2024; Vieira et al., 1991). The data sets used in our study span almost 18 years, from 28/07/2005 to 21/05/2023. Previous work devoted to the study of the ocean tides in Lanzarote can be found in Benavent et al. (2012). The main goal of the present work aims to explain the sea level variations observed in JA at multi-year to decadal time scales to improve the non-tidal corrections in the sea level time series. The ground level is monitored using a GNSS permanent station located just above the tide gauge position (García-Cañada & Sevilla, 2005). The study of correlations between sea level and vertical GNSS displacement time series may also be used to identify possible volcano-tectonic signals as this laboratory is situated in an active area (Arnoso et al., 2024). In this way, Tammaro et al. (2021) investigated the oscillations of relative sea level through the analysis of decadal tide gauge records collected in the Gulfs of Pozzuoli and Napoli (Southern Italy). Other than a high-resolution model of the sea tides, they successfully extracted from the tide gauge records the volcano-tectonic signal (vertical ground displacement) in the resurgent Campi Flegrei caldera.

2. *Data Description and Preprocessing*

2.1. *Sea Level Series*

We used the sea level variations recorded in Jameos del Agua (JA) site (Fig. 1), from July 2005 to May 2023. The tide gauge used in this study is a high precision pressure sensor, SAIV A/S TD301R, co-operated by the Institute of Geosciences (IGEO, CSIC-UCM) and the Geodesy Research Group of the University Complutense of Madrid (GRG-UCM). The gauge is installed in a lake situated within a volcanic tube, as a result of the intersection with the

ocean on its path from La Corona volcano to the coast (Fig. 1b). Actually, the tube has several sections along its path from the volcano to the sea: a dry section, a partially flooded section and a submerged section (Fig. 1b, c). The lava tube has also several openings, some of them are skylights as a result of collapses in the roof of the tube. In local language, a skylight is named as *jameo,* which means a cavity in the ground (Carracedo et al., 2003). Several underwater speleological expeditions showed that the submerged section of the tube extends from the current coastline out the sea for about 1800 m. Sea water penetrates at least 600 m inland into the lava tube forming lakes through direct and indirect communication between the sea and the lava tube. The former occurs through a small hole in the submerged tube, 750 m offshore, and the latter from fissures, cracks and the porosity of the volcanic rocks (Martínez García et al., 2016). The ocean tides observed in the lakes showed sea tide elevations up to 1 m at the inner point furthest from the coastline (Arnoso, et al., 2001).

The raw tide gauge records require a careful quality control and data processing, carried out in four main stages: (a) visual inspection for a first-order quality control; (b) de-tiding and Dynamic Atmospheric Correction; (c) non-seasonal daily solution; (d) monthly averaging.

2.1.1 Quality Control

A standardized sea level quality control was applied to the raw data to check for bad data. In the first four years, there are up to 50% of missing data mainly produced by power supply failures. The longest gap for this period lasted about six months (2006/07/26 to 2007/01/23). From 2009 to 2019 missing data were reduced to 12%, and from 2020 to 2023 the data missing was less than 1%. Figure 2a shows the observed tide gauge data at JA, where the lake level range is of 2.47 m for the period of study. Figure 2b zooms year 2021 to highlight the diurnal tidal range. In the following, a more detailed quality control based on outlier detection and tidal analysis is performed. Furthermore, with the aim of performing an additional validation of the sea level time series at JA site, comparisons with three tide gauge stations located in different islands of the Canary archipelago were made (Supplementary Information).

2.1.2 De-tiding and Dynamic Atmospheric Correction (DAC)

Sea level data were analysed to filter out the tides and other high frequency oscillations. Data were processed using the VAV software (Venedikov et al., 2003, 2005), which uses least squares harmonic analysis to estimate the tidal parameters (amplitudes and phases). This software allows the calculation of the sea water temperature effect on the tidal data by applying a regression approach in the time–frequency domain. Furthermore, an automatic iterative process allows the detection of outliers through comparison of the residuals with a fixed threshold level of significance (2.5 times the standard deviation). Our analysis process ended after five iterations and the 3.4% of the hourly data were removed. This analysis guarantees the good quality of the data used in subsequent processing. Lanzarote has a predominantly semidiurnal tidal regime, with a shape factor of F = 0.1. The amplitudes for the M2 and O1 tidal waves obtained in the harmonic analyses were 60.14 ± 0.02 cm and 4.20 ± 0.01 cm, respectively. The estimated tidal phases have not been given because they depend on the lag induced by the lava tube and, therefore, they are not representative of the tidal phases in the coast.

Figure 2c shows the hourly sea level residuals after removing the tides from July 2005 to May 2023. We call this residual hourly non-tidal residual. The linear trends calculated at this stage show a decrease of 2.60 cm/yr rate, from 2005 to the beginning of 2009, whereas for 2009 to 2021 it increases at a rate of 1.92 cm/yr. It is worth to mention the abnormal behaviour in the time series for the period comprised between February to May, 2022 (Fig. 2d), with a decrease of at most 15 cm, which could be amplified due to local conditions of the observing site in the lava tube.

For time scales of several days, most of the sea level variability becomes from the atmospheric forcing. The high frequency signal due to atmospheric effects (pressure and wind for periods shorter than 20 days) and the low frequencies of the inverted

barometer have been corrected from the hourly non-tidal residual using the DAC model (Carrère & Liard, 2003; Carrère et al., 2016) as per Oelsmann et al. (2024). The model, produced by CLS (Collecte Localisation Satellites, Toulouse, France) and distributed by Aviso + (https://www.aviso.altimetry.fr), is provided every 6 h over a global grid with spatial resolution of 0.25° × 0.25° (28 km × 28 km). In this study, DAC data were interpolated to the tide gauge location by using the nearest grid point method and resampling linearly to construct an hourly time series for the 2005–2023 period (Fig. 2). We call the resulting time series hourly non-tidal residual DAC corrected.

2.1.3 Non-seasonal Daily Solution

We filtered out the remaining high frequency energy by applying a 119-point convolution filter (Blomfield, 1976), to calculate daily values of sea level from the hourly non-tidal residual DAC corrected. Subsequently, we applied a multivariate linear least squares adjustment to remove annual and semi-annual components of the seasonal sea level cycle, resulting:

$$y_2(t) = y_1(t) - \hat{A}_1 \cos(\omega_1 t) - \hat{A}_2 \sin(\omega_1 t) - \hat{A}_3 \cos(\omega_2 t) - \hat{A}_4 \sin(\omega_2 t) \quad (1)$$

where $y_1(t)$ denotes the filtered daily values, ω_1 and ω_2 are the annual and semi-annual frequencies, respectively, and the $\widehat{A}_1$, $\widehat{A}_2$, $\widehat{A}_3$ and $\widehat{A}_4$ denote the estimated coefficients in the linear fit.

It should be noted that annual and semi-annual components were not removed in the tidal analysis procedure as these frequencies have, in addition to the tide, an important meteorological contribution. Therefore, we include these components to be removed after the DAC correction and the daily filtering. The estimated amplitudes of semi-annual and annual component were found 1.70 ± 0.09 cm and 0.84 ± 0.08 cm, respectively.

2.1.4 Monthly Averages

The average monthly time series were calculated by the following procedure:

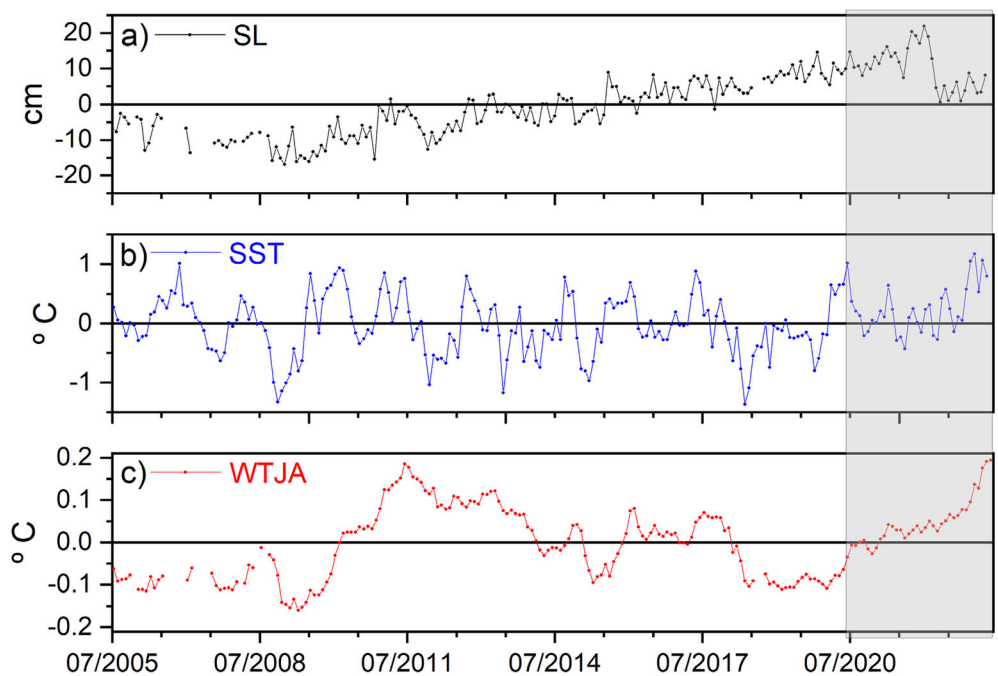

Figure. 3
Deseasoned monthly averages for sea level at JA site **a**, sea surface temperature outside the lava tube **b** and water temperature in the lake within the lava tube **c**. The grey area highlights the last three years of records

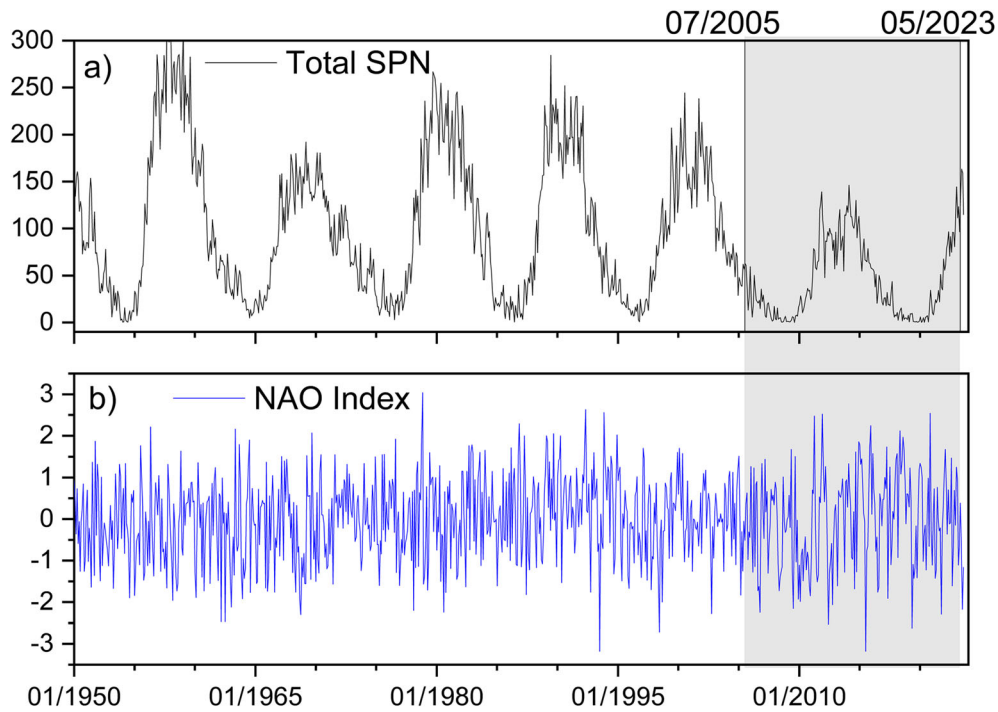

Figure. 4
a Monthly mean values of total sunspot number, from 1950 to 2024. **b** For the same time period as in a), the NAO Index time series. The grey area highlights the common period with the sea level data used in this work (July 2005 to May 2023)

1) For each month, we calculated the simple average from the non-seasonal daily solution given by (1) and denoted as $m(t) \equiv m_{ij}$, where subindex correspond to i th month of the year and j th year of the time series ($j = 1, \ldots N$).

2) The computation of the common monthly component or mean annual cycle was carried out by means of stacking, that is, by averaging for each month of the year, i, over the whole time series:

$$m_i = \frac{\sum_{j=1}^{N} \boldsymbol{m_{ij}}}{N} \tag{2}$$

3) Finally, the common component is subtracted to the corresponding value to get average monthly sea level anomalies:

$$y_3(t_{ij}) = m_{ij} - m_i \tag{3}$$

Hereafter we refer to this result as 'deseasoned sea level monthly average'.

2.2. Sea Water Temperature

We consider two different data sets of water temperature: the first one, Water Temperature at Jameos del Agua (WTJA), corresponding to in situ temperature in the lake. The second one, Sea Surface Temperature data (SST), outside the lava tube (in the open ocean), was obtained from the Hadley Centre Sea Ice and Sea Surface Temperature data set (Online document Met Office, Hadley Centre, HadISST 1.1. 2006; Rayner et al., 2003). SST data are binned products, with a resolution of 1°, generated from a blend of in-situ and adjusted satellite measurements. We used monthly means at the centre of the grid cell closer to JA site (coordinates 13.5° W, 29.5° N, see Fig. 1). This cell lies just on the border of the oceanic area of the North Atlantic subtropical gyre and the coastal upwelling zone.

From July 2005 to May 2023, the average value of in-situ seawater temperature is about 18.9 ± 0.1 °C, and the one of SST is about 20.8 ± 1.8 °C, respectively. For both cases, WTJA and SST, the mean

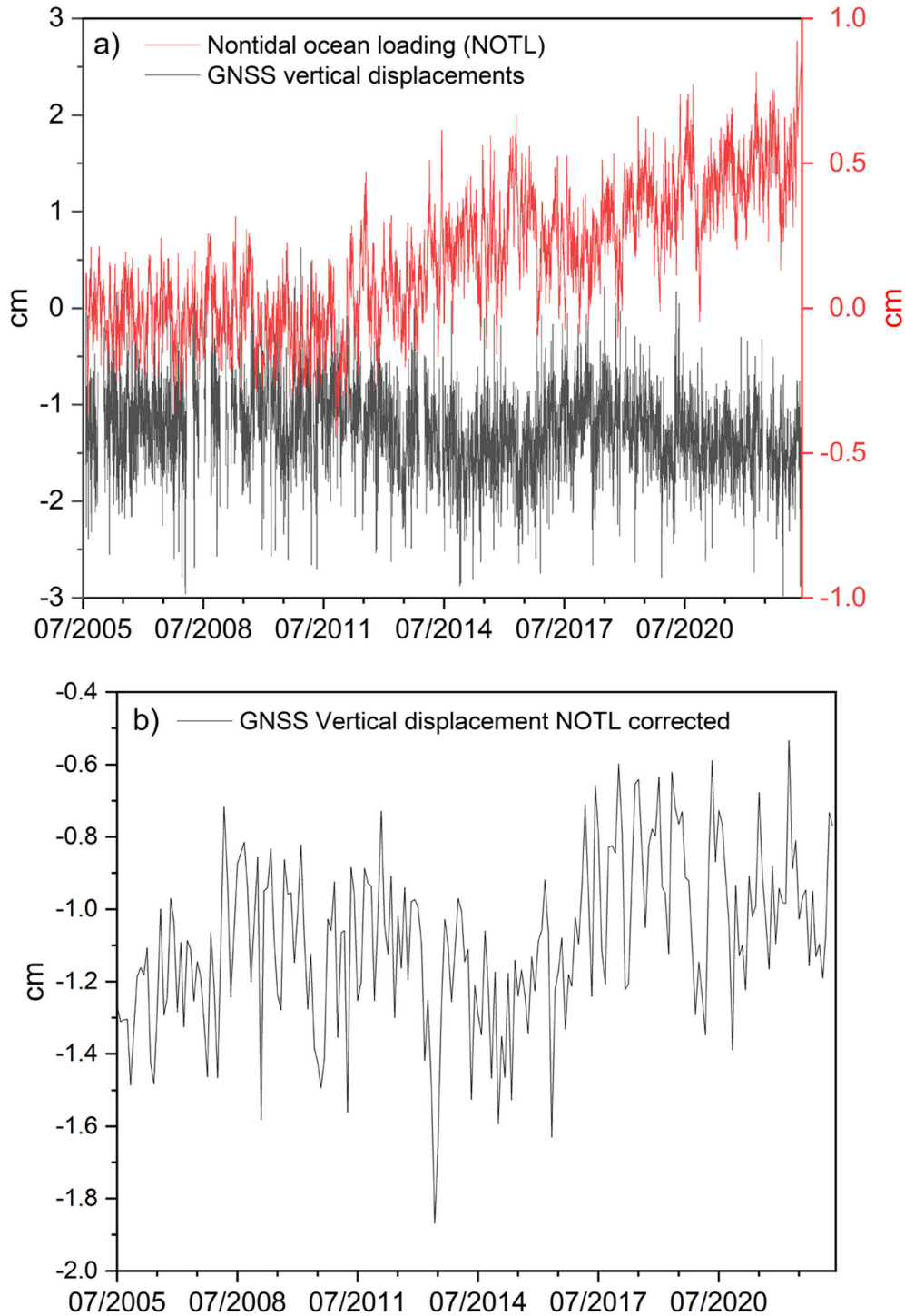

Figure. 5

a GNSS-vertical displacement (black line) processed without non-tidal loading correction. The red line shows the variations of the NTOL displacement at LACV station derived from ECCO2 model. **b** Monthly GNSS-vertical displacement series with NOTL corrected

annual cycle has been removed from the monthly averages, following the same procedure explained for sea level data in Sect. 2.1.4. We call them deseasoned WTJA and SST monthly averages (Fig. 3), respectively.

2.3. Sunspot Number

We use the sunspot number (SPN) to study the solar influence on sea level. This value is the only direct record available for studying the solar variability on solar cycle timescales as well as the long-term influence of the Sun on the Earth's environment (Clette et al., 2014). In particular, monthly data are calculated from arithmetic means of the daily total sunspots number over all days each month, being the daily total relative sunspots number R calculated as (e.g., Veronig et al., 2021):

$$R = N_S - 10N_g \tag{4}$$

N_S being the total number of sunspots and N_g the number of sunspots groups.

The SPN data are retrieved from the Solar Influences Data Analysis Center of the Royal Observatory of Belgium (https://www.sidc.be/SILSO/home). Figure 4 shows the monthly sunspot number for the period 1950–2023 to show its long-term variability.

2.4. North Atlantic Oscillation

In the northern hemisphere one of the most important atmospheric modes of variability, understood these as spatial patterns and its fluctuations across different time scales (see e.g., Hernández et al., 2020; Lombard et al., 2005), is the North Atlantic Oscillation (NAO). NAO represents a large-scale atmospheric circulation pattern that can cause changes of a few centimetres in sea level at annual time scales in some areas (Tsimplis et al., 2013). Several authors have studied the time scale variability of the nonstationary NAO behaviour. For example, Fritier et al. (2012) emphasized the $\sim$ 18-year scales of variability characterizing the period covering 1970 to 2000 or the inter-annual variability of $\sim$ 6-year characterizing the late 1980s to early 2000.

We used the NAO Index, which is defined as the normalized pressure difference between Azores and Iceland, to study its possible long-term relationship with the observed sea level at JA site. The monthly time series of the NAO index were obtained from the Climate Prediction Center of the National Weather Service (NOAA, https://www.cpc.ncep.noaa.gov/products/precip/CWlink/pna/nao.shtml). We used all data available, from 01/1950 to 05/2023 (Fig. 4).

2.5. GNSS-Vertical Displacement

The sea level measured at JA site is relative to a land-based benchmark that is locally tied to a permanent GNSS station named LACV, which is located just above the tide gauge site, in the roof of the lava tube (Fig. 1c; Fig. 5). LACV station (managed by CSIC-UCM and GRG-UCM) has been operating since 1999 and takes part of a small GNSS network spanning the island of Lanzarote to study ground deformations and to understand the active tectonics of the island (Riccardi et al., 2018). GNSS data refer to the same period as the sea level records (2005– 2023). We used the Canadian Spatial Reference System Precise Point Positioning (CSRS-PPP) online service of the Natural Resources of Canada (https://webapp.csrs-scrs.nrcan-rncan.gc.ca/geod/tools-outils/ppp.php) to provide the daily solutions of the vertical displacement. The CSRS-PPP service computes the standard Precise Point absolute Positioning (PPP) for GNSS measurements prior to 2018. By means of this processing the observables (P-code and phase shift) are modelled by forming double differences of a linear free ionospheric combination. For data collected from 2018 onwards, the PPP processing technique is modified to include a reliable integer ambiguity resolution (PPP-AR, Banville, 2020). Both methods, PPP and PPP-AR, use accurate satellite orbit and clock information from the IGS GPS service, absolute calibration models for antenna phase centre variation and include corrections for other geophysical effects such as earth tides, ocean tide loading and pole tide (IERS Conventions, 2010). The daily GPS positions are referred to the IGS20/ITRF2020 (https://igs.org/news/igs20/).

As for the case of sea level, seasonal and annual fluctuations were removed from the daily GNSS-

vertical displacements time series to accurately estimate long-term linear trends. It has been shown that most of this type of observed oscillations on GNSS series can be explained by non-tidal ocean loading effects (NTOL) that have not been corrected during the GNSS data processing (Williams & Penna, 2011; Zerbini et al., 2004).

The NTOL is due to variations in the ocean bottom pressure by the sea surface height variability and by density variations in the water columns (van Dam et al., 1997). The vertical displacement produced by NTOL effect can be computed by convolving an ocean global bottom pressure model with the Green's functions for a given earth's model. In this study, we used the NTOL surface displacement series estimated from the ECCO2 (Estimating the Circulation and Climate of the Ocean Phase II, Menemenlis et al., 2008) model, which is distributed by the EOST Loading Service (http://loading.u-strasbg.fr/index.php) with a spatial resolution of 0.25° for 24 h sampling intervals.

After correcting NTOL from daily displacements, we removed annual and semi-annual components by least squares fitting, similarly to Eq. (1), and subtracted a mean annual cycle to get monthly averages, in an equivalent way as Eqs. (2) and (3). Figure 5b shows this final corrected time series.

3. Methods

3.1. Multi-Resolution Analysis Based on the Maximal Overlap Discrete Wavelet Transformation

We applied the Multi-Resolution Analysis based on the Maximal Overlap Discrete Wavelet Transformation (MRA-MODWT) to study other non-tidal signals and non-stationary components at different frequencies in the time series (sea level, sea temperature, sunspot and NAO index).

The multi-resolution analysis (MRA) consists of an additive decomposition of the signal into different scales of variations using a suitable wavelet transformation, while preserving the location of the distinct features (zero phase property). That is, the signal $\boldsymbol{X} = (X_0, \ldots, X_{N-1})^T$ (a vector column containing the N observations of the time series) is expressed as the sum of $J + 1$ new series or levels, each of which related to variations at a certain scale (Percival & Mofjeld, 1997)

$$\boldsymbol{X} = \sum_{j=1}^{J} \widetilde{\boldsymbol{D}}_j + \widetilde{\boldsymbol{S}}_{\boldsymbol{J}} \tag{5}$$

For each j = 1, . . ., J; $\widetilde{\boldsymbol{D}}_j$ represents a time series, called j^{th} *level detail*, describing variations at successive dyadic scales τ_j. $\widetilde{\boldsymbol{S}}_J$ is a signal describing the low-frequency variation, changes over the scale τ_{J+1} or higher, called *smooth* or *approximation level*.

As wavelet transformation technique we used the Maximal Overlap Discrete Wavelet Transformation (MODWT). Thus, appropriate high and low pass filters split the frequency spectrum of the original signal into wavelet and scaling coefficients, by circular convolution within the Fourier domain (Rizvi et al., 2024; Whitcher et al., 2000). The main advantages of the MODWT are the translation-invariance and the zero-phase properties.

Hereafter the MRA-MODWT method is briefly summarized. Let be L, with $L \leq N$, the length of base filter ($j = 1$) from a wavelet family:

- $\widetilde{\boldsymbol{h}}_1 = \left(\widetilde{h}_{1,0}, \ldots, \widetilde{h}_{1,L-1}, 0, \ldots, 0\right)^T$ denote the namely rescaled wavelet filter coefficients, with $\widetilde{h}_{1,k} = 0$ for $L \leq k \leq N$, and $\widetilde{h}_{1,k}$ obtained by renormalizing the Discrete Fourier Transformation (DFT) filter $h_{j,k}$ of the wavelet family: $\widetilde{h}_{j,k} = h_{j,k}/2^{j/2}$.
  The corresponding scaling filter coefficients, $\widetilde{\boldsymbol{g}}_1 = \left(\widetilde{g}_{1,0}, \ldots, \widetilde{g}_{1,L-1}, 0, \ldots, 0\right)^T$ are:

$$\widetilde{\boldsymbol{g}}_{1,\boldsymbol{k}} = (-1)^{k+1} \widetilde{\boldsymbol{h}}_{1,\boldsymbol{L-1-k}} \tag{6}$$

- For $n = 0, \ldots, N-1$, the DFT of $\widetilde{\boldsymbol{h}}_1$ is given by:

$$\widetilde{\boldsymbol{H}}_{1,\boldsymbol{n}} = \sum_{\boldsymbol{k}=0}^{\boldsymbol{N-1}} \widetilde{\boldsymbol{h}}_{1,\boldsymbol{k}} \boldsymbol{e}^{-\frac{i2\pi k}{N}} \tag{7}$$

and, similarly, $\widetilde{G}_{1,n}$ denotes the DFT of $\widetilde{\boldsymbol{g}}_1$.

Thus, the wavelet filters $\widetilde{\boldsymbol{h}}_{\boldsymbol{j}}$ and $\widetilde{\boldsymbol{g}}_j$ for the scales $\tau_j = 2^{j-1}$ and $2\tau_J = 2^J$, respectively, are defined as the inverse DFT:

$$\widetilde{\boldsymbol{H}}_{\boldsymbol{j},\boldsymbol{n}} = \widetilde{\boldsymbol{H}}_{1,2^{j-1}\boldsymbol{n}\bmod N} \prod_{l=0}^{j-2} \widetilde{\boldsymbol{G}}_{1,2^{l}\boldsymbol{n}\bmod N} \tag{8}$$

$$\widetilde{\boldsymbol{G}}_{\boldsymbol{J},\boldsymbol{n}} = \prod_{l=0}^{J-1} \widetilde{\boldsymbol{G}}_{1,2^{l}\boldsymbol{n}\bmod N} \tag{9}$$

for $n = 0, \ldots, N-1$.

Then, the MODW wavelet and scaling vectors are constructed from the $\boldsymbol{\chi}_n = (\chi_0, \ldots, \chi_{N-1})^T$ DFT of $\boldsymbol{X}$ calculating:

- For $j = 1, \ldots, J$, the coefficients column vector of length N, $\widetilde{\boldsymbol{W}}_j$, as the inverse DFT of $\{\widetilde{H}_{j,n}\chi_n\}$ associated with scale changes of τ_j. The j^{th} filter coefficient has width $L_j = (2^j - 1)(L-1) + 1$.
- The coefficients vector $\widetilde{\boldsymbol{V}}_J$ as the inverse DFT of $\{\widetilde{G}_{J,n}\chi_n\}$, associated with scale changes of 2 τ_j or higher.

In practice, the jth wavelet and scaling filter coefficients are calculated from the scaling coefficients of level j -1, using an iterative algorithm (see, for example, Appendix A in Percival & Mofjeld, 1997).

Finally, the elements of $\widetilde{\boldsymbol{D}}_j$ and $\widetilde{\boldsymbol{S}}_J$ in Eq. (5) are obtained by filtering $\widetilde{\boldsymbol{W}}_j$ directly with $\widetilde{\boldsymbol{h}}_{\boldsymbol{j}}$ and with $\widetilde{\boldsymbol{g}}_{\boldsymbol{J}}$, respectively. It can be shown that MODWT is energy conserving (Percival & Walden, 2000)

$$\|\boldsymbol{X}\|^2 = \sum_{j=1}^{J} \|\widetilde{\boldsymbol{W}}_j\|^2 + \|\widetilde{\boldsymbol{V}}_J\|^2 \tag{10}$$

although $\|\boldsymbol{X}\|^2 \neq \sum_{j=1}^{J} \|\widetilde{\boldsymbol{D}}_j\|^2 + \|\widetilde{\boldsymbol{S}}_J\|^2$ the value $\|\widetilde{\boldsymbol{W}}_j\|^2$ can be considered as the contribution to the square norm of $\boldsymbol{X}$ of variations associated with scale τ_j and, equivalently, $\|\widetilde{\boldsymbol{V}}_J\|^2$ the contribution due to changes at scales 2 τ_j and higher. Thus $\|\boldsymbol{X}\|^2$ is referred as the energy of the time series, and $\|\widetilde{\boldsymbol{W}}_j\|^2$ and $\|\widetilde{\boldsymbol{V}}_J\|^2$ as the relative energy for the j and J levels, respectively.

3.2. *Cross-Wavelet Transformation and Wavelet Coherence*

The cross-wavelet transform of two time series provides areas with high common power and the relative phase in time–frequency space of the series. Denoting by W_n^x and W_n^y the continuous wavelet transform for each time series, x_n and y_n (n = 0,1, ... N–1), the cross-wavelet transform is formally defined as (Grinsted et al., 2004; Torrence & Compo, 1998)

$$\mathrm{W}_n^{xy}(s) = \mathrm{W}_n^x(s)\mathrm{W}_n^{y*}(s) \tag{11}$$

s being the wavelet scale and the (*) denoting complex conjugate.

As $\mathrm{W}_n^{xy}(s)$ is a complex number, it is possible to calculate the cross-wavelet power as $\left|\mathrm{W}_n^{xy}(s)\right|$ and the relative phase of the series in the time–frequency space from its complex argument $\arg\left(\mathrm{W}_n^{xy}\right)$.

Subsequently, a measurement of how coherent is the cross-wavelet transform in the time–frequency space is provided by the wavelet coherence. The squared wavelet coherence is defined as the square of the cross-spectrum normalized by the individual wavelet spectrum of each signal (Grinsted et al., 2004)

$$\mathrm{R}_n^2(s) = \frac{\left|s^{-1}\left\langle W_n^{xy}(s)\right\rangle\right|^2}{\left\langle s^{-1}\left|\mathrm{W}_n^x(s)\right|^2\right\rangle\left\langle s^{-1}\left|\mathrm{W}_n^y(s)\right|^2\right\rangle} \tag{12}$$

The angular brackets denote a smoothing operator, in both time and scale, and the factor s^{-1} is introduced to convert to an energy density. The wavelet coherence defined in this way takes values in the range [0,1].

The smoothing is carried out by convolution with a function depending on both the selected wavelet and the scale. For example, for the Morlet wavelet that we use in this paper, time smoothing is given by Gaussian function and the scale smoothing is a boxcar filter with a scale decorrelation length empirically determined of 0.6 (Torrence & Webster, 1999).

The phase coherence, which provides information about the possible delay in the relationship between the time series, is defined as:

$$\phi_n(s) = \tan^{-1}\frac{\mathrm{Im}\left(s^{-1}\left\langle W_n^{xy}(s)\right\rangle\right)}{\mathrm{Re}\left(s^{-1}\left\langle W_n^{xy}(s)\right\rangle\right)} \tag{13}$$

Re() and Im() being the real and imaginary parts of the cross-wavelet transform, respectively.

Since the time series are of finite length, errors occur in the wavelet power spectrum at the beginning and end of the series, and the larger the value of s, the larger the error. Thus, a namely *cone of influence* is introduced to delimit the regions of the wavelet

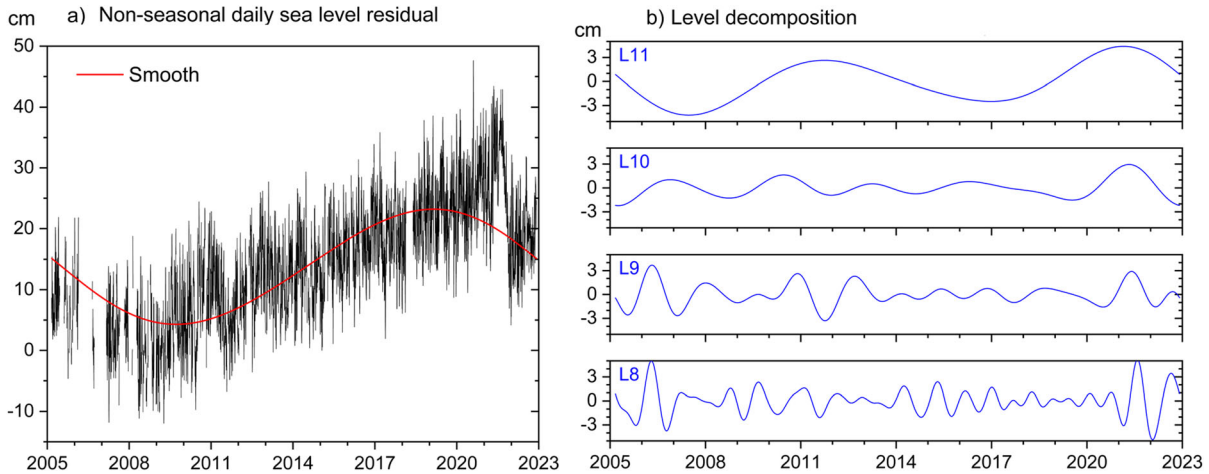

Figure. 6
a Non-seasonal daily sea level residual (black line) and the smooth component obtained from the level decomposition of the signal. **b** Level decomposition L8 to L11 of the series, which comprises the periods ranging from 0.7 to 10.1 years

Table 1

Energy values of the non-seasonal daily solution in Eq. (1). Decomposition up to level 11 and the smooth component

Level	Period (years)	Relative energy (%) MODWT Coefficient
L1	0.0055 – 0.011	0.39
L2	0.0106 – 0.0227	0.52
L3	0.0212 – 0.0454	1.97
L4	0.0424 – 0.0909	1.67
L5	0.0848 – 0.1820	1.66
L6	0.170 – 0.363	1.37
L7	0.339 – 0.726	1.02
L8	0.678 – 1.450	1.40
L9	1.36 – 2.89	1.10
L10	2.71 – 5.87	0.82
L11	5.53 – 10.10	3.49
Smooth	13.6 – Inf	83.58

spectrum in which edge effects become more important. Finally, the significance level of the wavelet coherence can be estimated using Monte Carlo methods. Details on both the cone of influence calculation and the estimation of significance levels are given in Grinsted et al. (2004).

4. Results

4.1. MRA-MODWT Signal Decomposition

We applied the MRA-MODWT method described in Sect. 3.1 for the component separation of the signal into different frequency bands. For all series (sea level and complementary data: WTJA, SST, SPN and NAO Index) we adopted the Symlet wavelet family, circular boundary conditions, and the largest level was selected such as $J \leq \log_2 N$ (Cornish et al., 2006). Other suitable wavelets families were investigated for the different time series (such as Daubechies, Coiflets and Fejér-Korovkin wavelets). The small time-scale level decomposition had similar features, whereas the larger time-scale part using a Symlet looks smoother than the others. We choose the Symlet wavelet family (with sym4 filter of length 8) to ensure the smooth decomposed results. Thus, we decomposed the series in a smooth component and 11 levels (L1 to L11) for daily series and 6 levels (L1 to L6) for monthly ones.

The calculations for the MRA-MODWT were carried out with the *Signal Multiresolution Analyzer App* of MATLAB software (The MathWorks Inc., 2023). Figure 6 shows the non-seasonal daily residual, given by the Eq. (1), together with the smooth component and the last 4 levels obtained thorough the component separation, for the period 2005 to 2023.

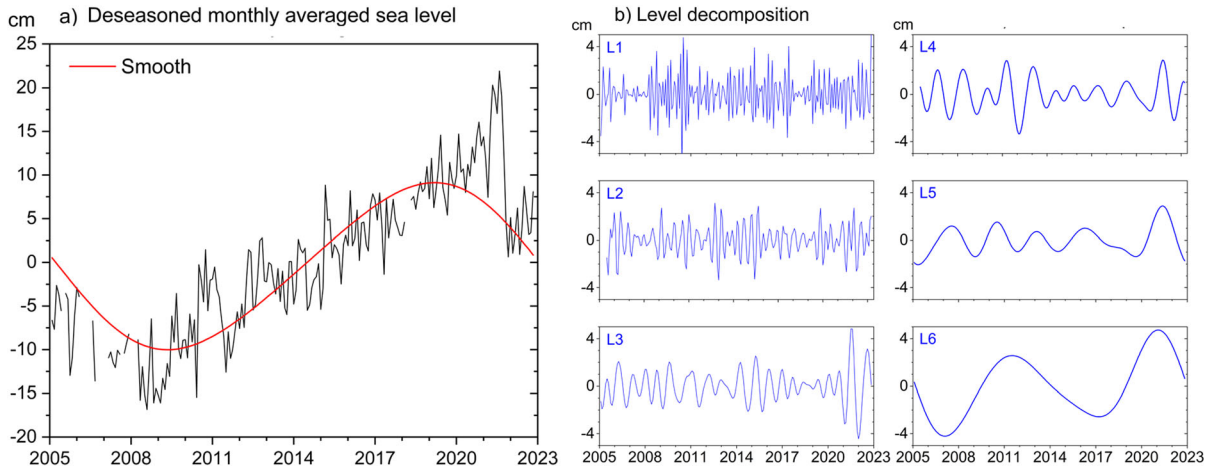

Figure. 7

a Monthly sea level residual (deseasoned monthly average, black line) and the smooth component (red line) obtained from the level decomposition of the signal. **b** Level decomposition (L1 to L6) of the series. The corresponding periods are given in Table 2

Table 2

Energy values of the sea level (deseasoned monthly average) decomposition up to level 6 and the smooth component

Level	Period (years)	Relative energy (%) MODWT Coefficient
L1	0.167 – 0.333	4.52
L2	0.321 – 0.691	3.47
L3	0.645 – 1.38	3.99
L4	1.29 – 2.74	3.65
L5	2.57 – 5.39	3.22
L6	5.19 – 10.1	13.87
Smooth	12.7—Inf	67.28

Table 1 lists the energy values of the decomposed levels, and the following can be highlighted:

– The smooth component, which represents low frequency variations higher than 13.6 years, comprises the 83.6% of the total energy of the signal. Within this level, part of a cyclic signal of 18 to 19 years periodicity was found.
– The level L11, with a 3.5% of the total energy, could show a signal with a period of about 9 to 9.5 years.
– The levels L6 to L10 correspond to frequencies ranging from 2 months to 5.5 years, comprising 5.7% of the total energy.
– The levels L5 to L1 correspond to frequencies from 2 days to 2 months, comprising 6.1% of the total energy.

It should be mentioned that monthly series are appropriate to analyse the signals included in the levels L1 to L10, as seasonal signals were already corrected. Similarly, Fig. 7 shows the deseasoned sea level monthly average given in Eq. (3), together with the smooth component and the six-level decomposition of the signal. The following can be noted (see Table 2):

– The smooth component could recover half cycle (valley-pick) of a signal of 18–19 years periodicity. In this case, the energy of the signal representing the frequency variations higher than 12.7 years is of 67.3%.
– The level L6, having a 13.9% of the total energy, could recover two cycles of a signal with a period of about 9 to 9.5 years.

The deseasoned sea level monthly average, where the seasonal cycle has been removed from the time series used, allowed us to focus more clearly on the following frequency bands:

– From $\sim$ 1.4 to 5.4 years (levels L4 and L5), with a 6.8% of the total energy of the signal, it reveals

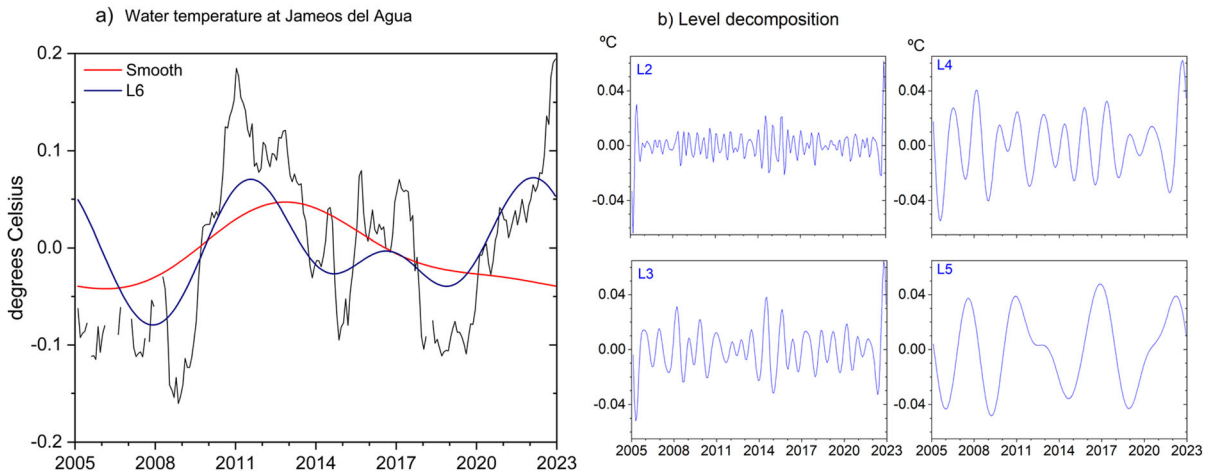

Figure. 8
a Deseasoned water temperature monthly average inside the lava tube (black line), the smooth component (red line) and the level L6 (dark blue line) obtained from the level decomposition of the signal. **b** Level decomposition (L2 to L5) of the series corresponding to the periods given in Table 3

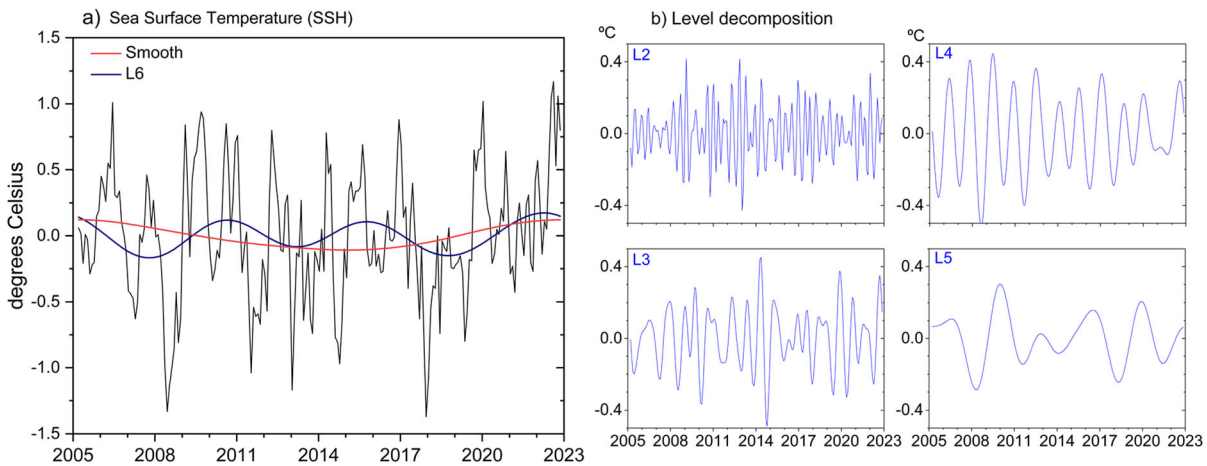

Figure. 9
a Deseasoned water temperature monthly average outside the lava tube (black line), the smooth component (red line) and L6 level (dark blue line) obtained from the level decomposition of the signal. **b** Level decomposition (L2 to L5) of the series corresponding to the periods given in Table 3

dominant periods of about 1.8 to 2 years and 2.5 to 3.5 years.

– From ∼ 2 days to 1.4 years (levels L1, L2 and L3), with a 12.0% of the total energy of the signal, it reveals dominant periods of about 3, 5 and 9 months.

We also repeated the same procedure to decompose the deseasoned sea water temperature monthly average series in the lake (WTJA) and in the open ocean (SST), the SPN and the NAO Index into 6 levels and a smooth component.

Figures 8 and 9 show the results for the WTJA and SST, respectively, together with the smooth component and the level L6. In both cases, the figures also show the last four decomposition levels (L2 to L5) obtained through the component

Table 3

Deseasoned WTJA and SST monthly average decomposition up to level 6 and the smooth component

		Relative energy (%) MODWT Coefficient	
Level	Period (years)	WTJA	SST
L1	0.167 – 0.333	1.31	10.35
L2	0.321 – 0.691	2.72	14.68
L3	0.645 – 1.38	6.57	22.76
L4	1.29 – 2.74	11.23	30.49
L5	2.57 – 5.39	20.25	12.04
L6	5.19 – 10.1	39.25	6.63
Smooth	12.7—Inf	18.67	3.03

separation. Table 3 lists the energy values of the decomposed levels, and it can be noted that:

- The levels L5 and L6 show signals with dominant periods of about 5 to 5.5 years and 3 to 3.5 years, respectively. These bands comprise 59.5% and 18.7% of the total energy for WTJA and SST, respectively.
- For L4 level, the energy reaches values of 11.2% for WTJA and up to 30.5% for SST, with dominant signals of 1.8 to 2 years period.
- For L2 to L3 levels, the WTJA and SST decomposition recover remarkable signals with periods of about 5 to 8 months.

Figure 10 shows the SPN signal decomposition together with the smooth component and the L6 level. A dominant signal with a period of approximately 9.7 years is found at L6. This figure also shows the last four decomposition levels (L2 to L5) obtained through the component separation. Table 4 lists the energy values of the decomposed levels.

As we mentioned in Sect. 2.4, NAO Index can exhibit a remarkable component of 18.5 years. Since long series of NAO Index data are available, we decomposed two series: from 2005 to 2023 and from 1950 to 2023. Table 4 lists the energy values of the decomposed levels obtained for both periods. Most relevant differences appear for the levels L1 to L3, which correspond to periodicities ranging from 2 to 8 months. For the levels L4 to L6 and the smooth component, the energy is similar for the two periods of time analysed. Figure 11 displays the original series of NAO Index and its decomposition for the level 6 and the smooth component (that comprises the 6% of the total energy), which we are particularly interested in.

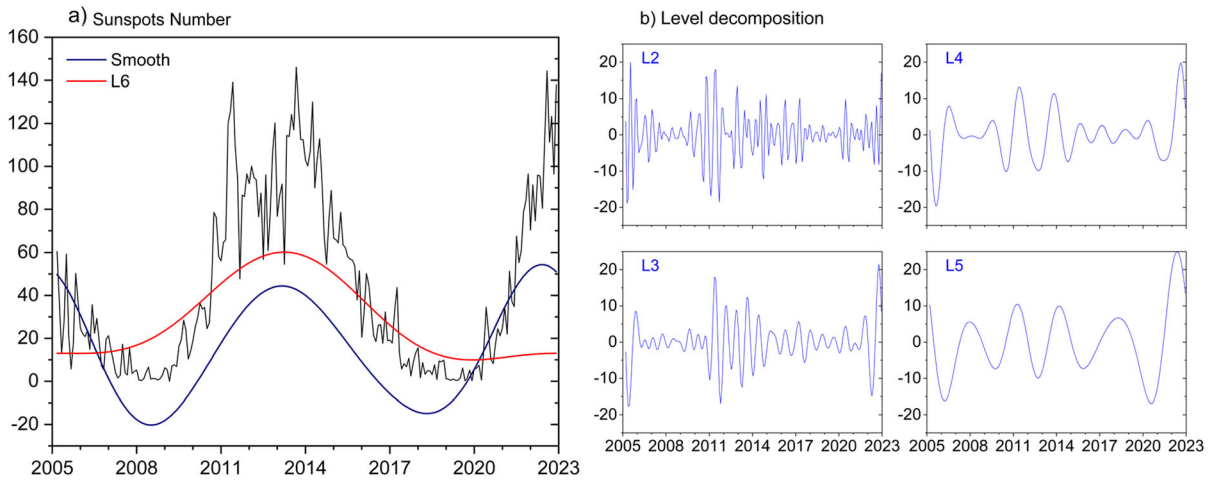

Figure. 10

a Deseasoned SPN monthly average (black line), the smooth component (dark blue line) and L6 level (red line) obtained from the signal decomposition. **b** Level decomposition (L2 to L5) of the SPN corresponding to the periods given in Table 4

Table 4

SPN and NAO Index time series decomposition up to level 6 and the smooth component. For NAO Index, two series of different length were decomposed: 18 years (2005–2023) and 73 years (1950–2023)

		Relative energy (%) MODWT Coefficient		
Level	Period (years)	SPN	NAO (2005–2023)	NAO (1950–2023)
L1	0.167–0.333	10.35	31.17	38.44
L2	0.321 – 0.691	14.68	21.61	25.66
L3	0.645 – 1.38	22.76	25.31	18.05
L4	1.29 – 2.74	30.49	11.58	8.21
L5	2.57 – 5.39	12.04	4.48	4.37
L6	5.19 – 10.1	6.63	1.24	1.42
Smooth	12.7—Inf	3.03	4.81	3.86

4.2. Time–Frequency Wavelet Analysis

We compared the sea level and the complementary data-series (WTJA, SST, SPN and NAO Index) through the calculation of cross-wavelet transformation and wavelet coherence, as it is explained in Sect. 3.2. The cross-wavelet transform allows to examine regions in time–frequency domain, sharing a large energy and/or with substantial phase relationship to suggest some causality between the series. We can consider the wavelet coherence as a correlation coefficient localized in the time–frequency space.

Following Grinsted et al. (2004), we considered the Morlet wavelet as the mother wavelet with a scale resolution of 10 scales per octave, because it provides a good balance between time and frequency when locating common features. The correlations between the sea level (deseasoned monthly average) and water temperature WTJA and SST by cross-wavelet and coherence analysis (Fig. 12) point out different periods of intra-annual variability (4–8 months) and inter-annual variability (approximately 2 and 2.5 years), from 2005 to 2017.

Although the WTJA and SST temperature series have different scales, both show a high correlation in the period of time analysed. The cross-wavelet transformation and wavelet coherence are shown in Figure S2.

The correlation analysis for sea level (deseasoned monthly average) and SPN shows, in the middle of the time scale, a statistically significant correlation from the of approximately 5.5-year variability scale. However, this low-frequency scale of variability must be interpreted with caution, as part of it falls out the cone of influence. The length of the sea level time series does not allow to establish correlation with NAO Index for the 18-year variability scale.

Arrows in Fig. 12 indicate the relative phase relationship between the time series. Arrows pointing right mean that both signals are in-phase (0 delay) while to the left signals have an anti-phase relationship (1/2 cycle delay). If arrows point down means 1/4 cycle lag between both signals. Thus, the significant sections of the cross-wavelet and coherence between the sea level (deseasoned monthly average) and WTJA and SPN series are in-phase for periods of 2.7 years. The coherence between the sea level and SST series are in-phase or present some phase shift, for periods of 1.3 to 2 years. Anyway, the phase is consistent and slowly varying. The significant sections of the wavelet coherence between sea level and NAO Index series, although are not in-phase or out-of-phase, present a consistent and slow varying phase for periods from 8 months to 2.7 years. For periods of 1.3 to 2 years, outside the areas with significant power the of series sea level and NAO Index are out-of-phase.

4.3. Further Modelling of Sea Level: A Regression Approach With Sea Water Temperature

With the information obtained in previous section, we reanalysed the original sea level data, after removing the effect of tides and DAC (this is the hourly non-tidal residual DAC corrected in Sect. 2.1). Then, we used the following regression approach (Arnoso et al., 2011; Ducarme et al., 2006; Venedikov et al., 2006):

$$y(t) = A(t) + E(t) + P(t) \tag{15}$$

The term $A(t)$ contains periods of 90 and 140 days, 2 and 2.5 years (intra-annual and inter-annual scales detected in the sea level, WTJA, SST and NAO Index decomposition). The term $E(t)$ is a

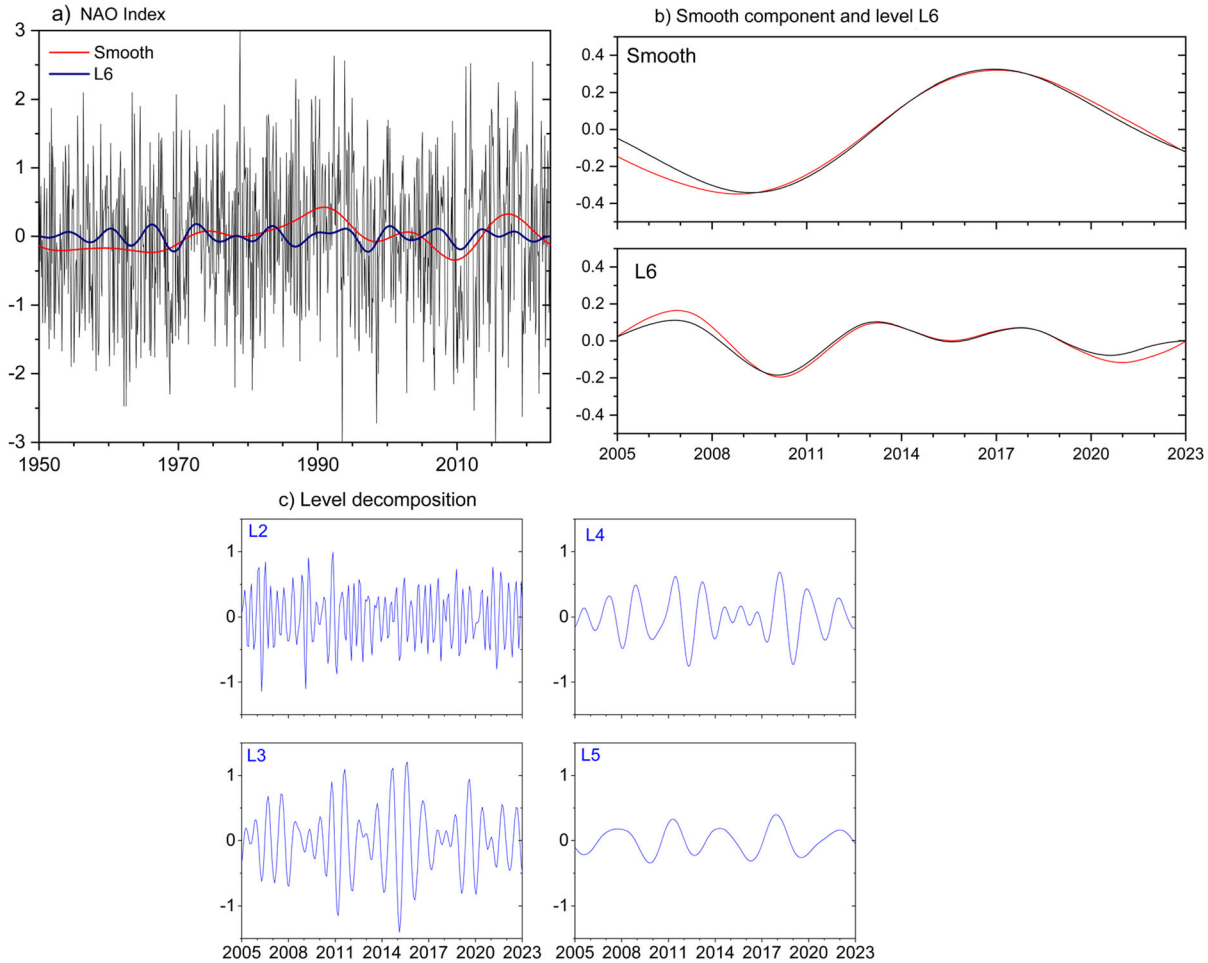

Figure. 11
a Deseasoned NAO Index monthly average and the smooth component (red line) and L6 level (dark blue line) obtained from the decomposition of the signal. **b** The smooth component and L6 level components obtained from NAO series for 1950–2023 (black line) and from 2005–2023 (red line). **c** Level decomposition (L2 to L5) of the NAO corresponding to the periods given in Table 4

component induced by the sea water temperature T as follows:

$$E(t) = R \cdot (T(t) - T_m) \tag{16}$$

R being the unknown regression coefficient and T_m the mean value of the water temperature in the lake. $E(t)$ is introduced to model the components detected with the wavelet coherence at several time-frequencies scales. The last term $P(t)$ is a polynomial of power 6, modelled as $P(t) = \sum_{k=1}^{6} c_k t_k$, and introduced here to improve the adjustment of $A(t)$ and $E(t)$.

Figure 13 shows the hourly time series component, $E(t)$. This term resulted from annual and biannual periods, and two longer ones of about 5.5 years and 9.5 years (which corresponds, approximately, to the sunspot cycle) as well as higher frequencies. $E(t)$ also validates the results obtained from wavelet coherence analysis for the sea level, water temperature and sunspot, as it was retrieved in Sect. 4.2. Therefore, we corrected the hourly non-tidal residual DAC corrected time series from the estimated $A(t)$ and $E(t)$ components. Subsequently, the non-seasonal daily solutions and monthly averages were calculated, as described in Sect. 2.

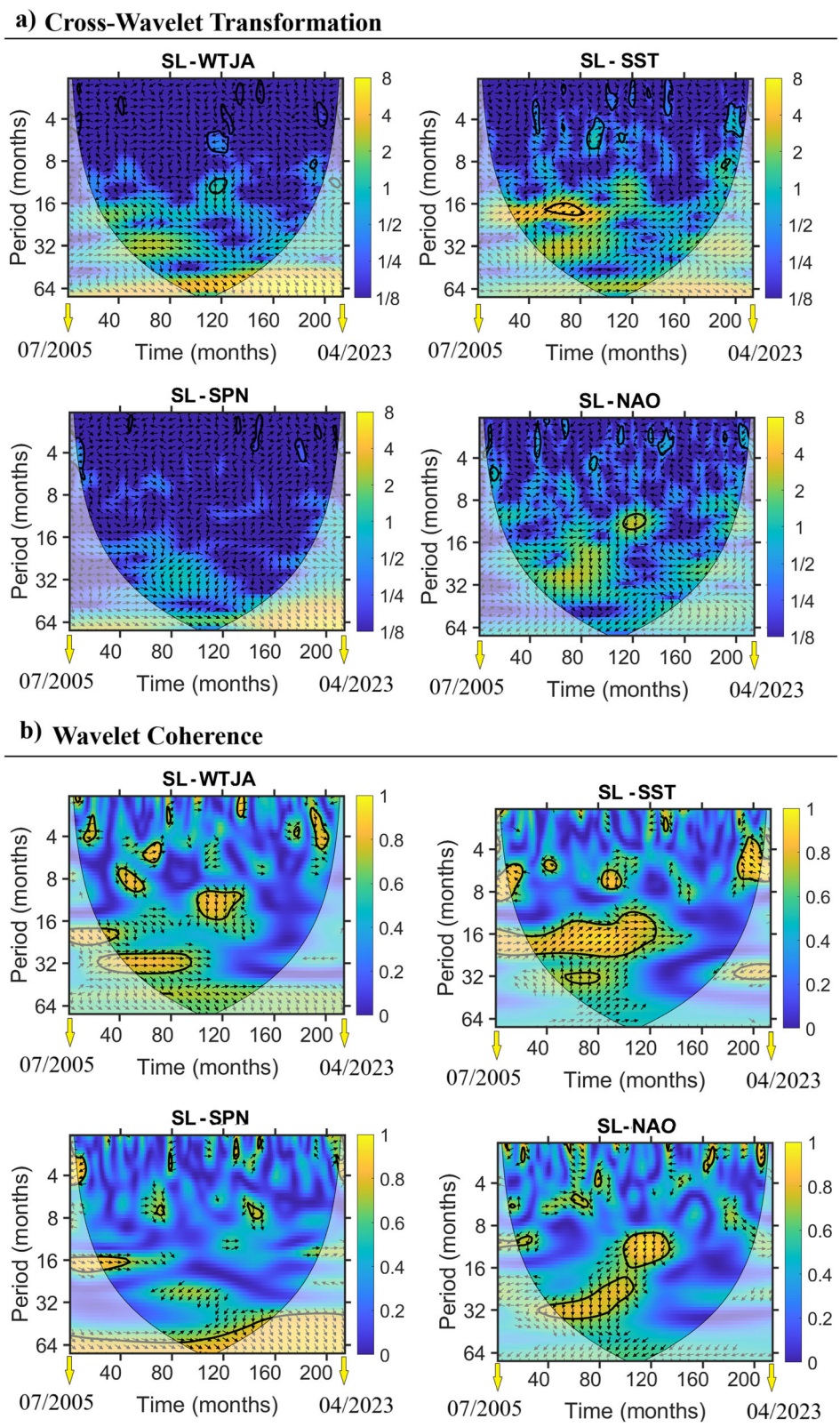
a) Cross-Wavelet Transformation
SL-WTJA
SL - SST
SL-SPN
SL-NAO
Period (months)
4
8
16
32
64
8
4
2
1
1/2
1/4
1/8
40
80
120
160
200
07/2005
Time (months)
04/2023
b) Wavelet Coherence
SL-WTJA
SL -SST
SL-SPN
SL-NAO
1
0.8
0.6
0.4
0.2
0

◀Figure. 12
Cross-wavelet and wavelet coherence analysis diagrams, for the time interval 2005 to 2023, for the sea level and WTJA **a,** SST **b**, SPN **c** and NAO Index **d**. Solid black lines represent the 95% confidence limit. All series correspond to deseasoned monthly averages

We applied all the corrections to the sea level time series based on the standard tidal corrections and the coherence study with the atmospheric and climate indexes. The resulting monthly residual (Fig. 14) still exhibits a component that could be part of a signal of about 18.5 years (the red curve is the smooth

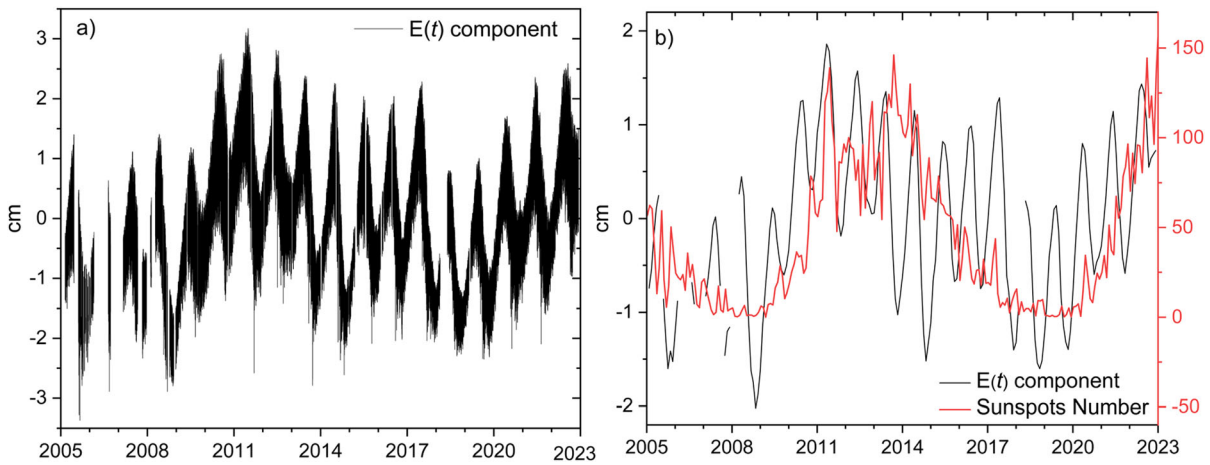

Figure. 13
a Hourly component $E(t)$ induced by the sea water temperature T as given by Eq. (16). **b** Monthly averages of the component $E(t)$ (black line) and the total SPN (red line)

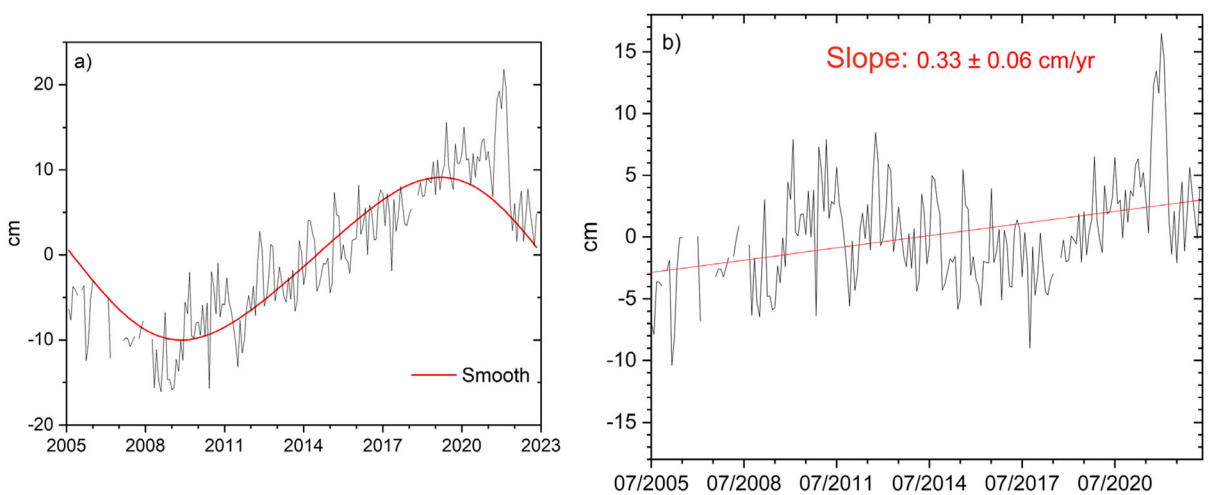

Figure. 14
a Deseasoned sea level monthly average with $A(t)$ and $E(t)$ components removed (black line) and its smooth component (red line). **b** Sea level residual in a) after the correction of the smooth component. The linear trend showed (red line) is calculated for the period July 2005 to May 2023

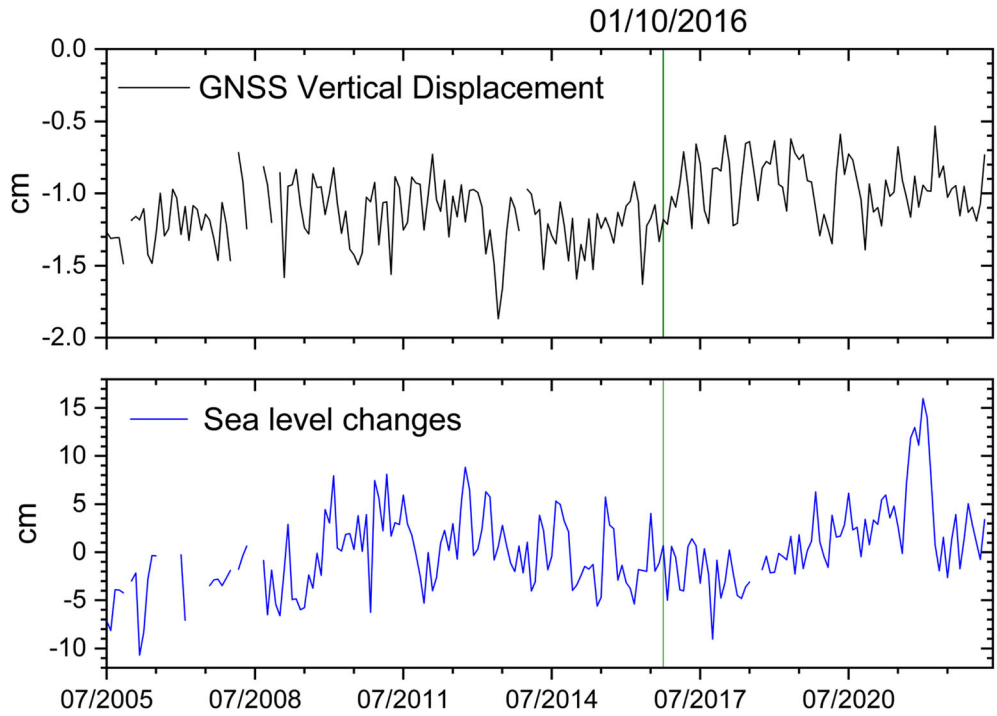

Figure. 15
Final sea level residual and GNSS-vertical displacement with NTOL correction applied. For the period July 2005 – May 2023, linear trends are 0.016 ± 0.003 cm/yr and of 0.33 ± 0.06 cm/yr for the GNSS-vertical displacements and the sea level residual, respectively. In October 2016 a significant ground uplift of about 0.3 cm can be observed (green line)

component determined by MRA-MODWT). The length of the time series does not allow to establish statistical correlations with other observables. However, from visual inspection, one can retrieve that it is close to the NAO Index smooth component for the same period of analysis (see Fig. 11). Furthermore, this period of about 18.5 year is close to the lunar nodal cycle, produced by the varying declination of the Moon over a period of 18.61 years. According to Pugh and Woodworth (2014) this is the main tidal force on decadal timescales and results in small variations of yearly averaged sea level (1–2 cm). Bult et al. (2024) unveiled that the lunar nodal cycle also has an influence on the temperature and salinity, and as a result on the steric sea level changes along the western European coast.

Consequently, we considered appropriate to subtract the smooth component (red line in Fig. 14a) to the sea level to get the final sea level residuals (Fig. 14b), which represent the sea level variations corrected for all the effects that could be identified. The calculation of the long-term linear trend provided an increase of 0.33 ± 0.06 cm/yr. This is in accordance with the values found for the sea level trend on a global scale (Elneel et al., 2024; Marrero-Betancort et al., 2022) and, in particular, in the Canary Islands region (Vargas-Yáñez et al., 2023).

5. *Discussion*

The considerable length and quality of the sea level records and the availability of complementary data from the JA site in Lanzarote Island, allows identifying components related with atmospheric and climatic effects. Therefore, we looked for new strategies to identify and model these components, so that they be accurately removed from the observations and subsequently achieving precise values of the long-term linear trends.

After applying standard tide (contribution of diurnal and semi-diurnal harmonic constituents of

189 cm) and seasonal non-tidal corrections to the observed sea level in JA, we performed a level decomposition of the monthly residuals through MRA-MODWT. We also applied a similar decomposition of the sea water temperature, the sunspot number and the NAO Index. As a result:

- We found levels containing a significant contribution to the total energy of sea level and water temperature signals (see Tables 2 and 3). On the one hand, levels with dominant components of about 2–2.5 year (L4 to L5 levels) and, on the other hand, levels with components of about 5 to 8 months (L1 to L3 levels). This fact implies that sea level (deseasoned monthly average) still retained a significant intra-annual and inter-annual contributions that could be correlated with the sea water temperature.
- The last level of the decomposition of the sea level series, L6 (see Table 2), contains a signal with a specific period of about 9 to 10 years. This component is relevant as it could be related to a similar component (period of approximately 9.7 years and at the L6 level) of the sunspot signal decomposition.

We applied the cross-wavelet transform and wavelet coherence approaches to corroborate the correlation found between the sea level and the complementary data obtained with the MRA-MODWT modelling. We subsequently used such information to model the sea level observation including a linear regression of the effect of sea water temperature. The main outcomes are the following:

- We obtained correlation between the final sea level residuals and sea water temperature and NAO Index for periods of 3 and 5–6 months, and 2 and 2.5 years (Fig. 12). This variability originates from seasonal warming and atmospheric pressure and wind (Biguino et al., 2024; Tsimplis et al., 2013). We included those periodic components as $A(t)$ in Eq. (15) and, as result, the estimated contribution is of 5.9 cm.
- We found a significant correlation between sea level and sunspots for a period of about 5.5 and 9.5 years. For these periods, correlation between solar activity and surface air temperature can be established (Le Mouël et al., 2020). It is therefore reasonable to assume that cyclic warming has effects on inter-annual variability of sea level observations. Estimation of these components through the term $E(t)$ in Eq. (16) amounts 6.5 cm.
  - o After removing $A(t)$ and $E(t)$, filtering sub-daily frequencies (e.g. wind, surges, high frequency tides) and suppressing of annual and semi-annual components (with an estimated contribution of 0.53 cm and 1.62 cm, respectively), the range of the residual sea level becomes 54.7 cm. This value is reduced to 37.9 cm when we compute the deseasoned monthly averages.
- Finally, we catch a glimpse on a smooth component of about 18.5 years in the sea level decomposition. However, due to the length of the available time series we cannot establish statistically significant correlation with other observables. After modelling of the smooth component of NAO Index and compare it with the sea level one (Figs. 11 and 14a) it appears that this effect contributes to sea level variations, in addition to the long-period astronomical tide (Pugh & Woodworth, 2014). Therefore, we removed the smooth component from the sea level records to further estimate its trend. The range of the final sea level residual is 26.9 cm. However, further long-term observations become necessary for assessing this component.

The sea level measured at the JA site is relative to a fixed, land-based benchmark locally tied to the GNSS station LACV (Fig. 5). This station is designed to control the stability of the benchmark, providing information on vertical land movements that could cause the variations of the sea-level. Therefore, we analysed the GNSS-vertical component to decipher any earth's surface deformation that can induce a particular variation in the observed sea level series. Results show that the effect of non-tidal loading on the GNSS-vertical component is substantial and causes a downward trend of this component (black curve in Fig. 5). We found a value of −0.020 cm/yr for the complete series and, once the NTOL effect is removed, it turns out to be about 0.016 cm/yr. With regard to the long-term linear

trends in the GNSS series, it is worth noting two specific periods. The first one comprises the period from July 2005 to October 2016 and the second one covers from October 2016 to May 2023. For these periods we obtained the values -0.005 ± 0.006 cm/yr and -0.01 ± 0.01 cm/yr, which denote an almost unnoticeable displacement. However, a remarkable ground uplift of about 0.3 cm was found from October, 2016 to January, 2017 (Fig. 15). Besides, the series of GNSS-vertical displacement and final sea level residual shows a good time correlation (Figure S3), so that a vertical land displacement implies a response in the observed sea level at JA site.

6. Conclusions

We used 18 years of sea level and complementary data observed in Lanzarote Island to understand the non-stationary and long-term linear variations of the observed sea level. The quality control carried out in the tidal analysis, the detection of anomalous data and the methodology used make the quality of the series observed in the JA lake to be suitable for sea level studies. Moreover, considering the peculiarity of JA site, the result obtained becomes comparable to those from other sea level series in the Canary Islands region. The application of different analysis techniques allowed us to highlight different periodic components in the tide gauge signals. Furthermore, the joint analysis of sea level changes with several ancillary data (sea water temperature, sunspot number, NAO Index) paved the way to hypothesise a possible origin or to detect possible forcing of the observed components. The main outcomes suggest that the intra and inter-annual variations of the sea level could be related to changes in the sea water temperature. A decadal variation of 9.5 years found is related to the solar cycle (Schwabe cycle). An almost inter-decadal variation was found and could be related to long period tides (the 18.5 year Lunar nodal cycle) and effects associated to NAO Index, although the data length does not allow to determine their contribution. Clearly, if the smooth component of the sea level decomposition is not removed the computed linear trend results strongly influenced by this component. Understanding this long-term variability is pivotal because it could improve our capability to detect possible acceleration in local sea-level rise due to global warming. Thus, with these considerations, the sea level trend estimated for the JA lake is 0.33 ± 0.06 cm/yr for the period 2005–2023, which is in agreement with other studies for the Canary Islands.

Regarding the earth's surface displacement analysed through the GNSS-vertical component of the reference station LACV, we have not found any remarkable linear variation for the period 2005 to 2016. From October 2016 to January 2017, we detected an uplift of 0.3 cm, although there is no induced effect in the sea level series for this short time period. Since January 2017, GNSS series does not exhibit a noticeable surface deformation, whereas the sea level trend after the smooth component of the sea level decomposition is removed presents a remarkable increase of 1 cm/yr.

Finally, our study of non-stationary components may help to identify more accurately non-linear trends of the sea level observed in Lanzarote Island. This is important for studies related to sea level connection to climate changes taking into account its complex temporal patterns, and also that its behaviour is not spatially uniform. This fact highlights the importance of maintaining long-term GNSS series simultaneously with sea level records.

Acknowledgements

This research has been supported by grant PID2019-104726GB-I00/AEI/https://doi.org/10.13039/501100011033 of the Spanish Research Agency. The authors are thankful to the Council of Lanzarote Island and also to the staff of Casa de los Volcanes, Jaime Arranz and Orlando Hernández, for providing us permanent technical support in the Geosciences Laboratory of Lanzarote. We would like to thank the Reviewers for their efforts in reviewing the manuscript. We sincerely appreciate all their valuable comments and suggestions, which helped us to improve the quality of the manuscript.

Author contributions MB and JA, conceptualization and methodology; JA, MB and UR, formal analysis and validation;

JA, MB, EV, FG, UT and UR, investigation and data curation; MB and JA, writing—original draft preparation; MB, JA, EV, FG, UT and UR, writing—review and editing; JA. and FG, project administration and funding acquisition. All authors have read and agreed to the published version of the manuscript.

Funding

Open Access funding provided thanks to the CRUE-CSIC agreement with Springer Nature. This research has been partially supported by the grant PID2019-104726 GB-I00/AEI/https://doi.org/10.13039/501100011033 of the Spanish Research Agency.

Data availability

The SST data are collected, processed and distributed by the National Center for Atmospheric Research and are available at https://www.metoffice.gov.uk/hadobs/hadisst/index.html (last access: 22 May 2024). The NAO index data were obtained from the Climate Prediction Center (NOAA) and are available at https://www.cpc.ncep.noaa.gov/products/precip/CWlink/pna/nao.shtml (last access: 22 May 2024). The Dynamic Atmospheric Correction (DAC) is produced by CLS and distributed by Aviso + , with support from CNES. Data are available at https://www.aviso.altimetry.fr/ (last access: 22 May 2024). The Sunspot Number are distributed by WDC-SILSO, Royal Observatory of Belgium, and are freely downloaded from https://www.sidc.be/SILSO/home (last access: 22 May 2024). The Tide gauge, water temperature and GNSS data from the Geodynamic Laboratory of Lanzarote (JA and LACV stations) were collected and produced by the IGEO (CSIC-UCM) and the UCM research Group 'Geodesy'. Data are available from the authors under reasonable request. All the graphics have been created using OriginPro from OriginLab corporation.

Declarations

Competing interests The authors declare no competing interests.

References

Arnoso, J., Benavent, M., Bos, M. S., Montesinos, F. G., & Vieira, R. (2011). Verifying the body tide at the Canary Islands using tidal gravimetry observations. *Journal of Geodynamics*. https://doi.org/10.1016/j.jog.2010.10.004

Arnoso, J., Fernández, J., & Vieira, R. (2001). Interpretation of tidal gravity anomalies in Lanzarote, Canary Islands. *Journal of Geodynamics, 31*, 341–354. https://doi.org/10.1016/S0264-3707(01)00003-5

Arnoso, J., Vélez, E. J., Montesinos, F. G., & Benavent, M. (2024). The geosciences laboratory of lanzarote. *International Workshop Geosciences in Active Areas*. https://doi.org/10.20350/digitalCSIC/16338

Banville, S., Geng, J., Loyer, S., Schaer, S., Springer, T., & Strasser, S. (2020). On the interoperability of IGS products for precise point positioning with ambiguity resolution. *Journal of Geodesy*. https://doi.org/10.1007/s00190-019-01335-w

Benavent, M., Arnoso, J., & Velez, E. J. (2012). *Tides at the East Coast of Lanzarote*. Geophysical Research Abstracts European Geosciences Union General Assembly.

Berrino, G. (1998). Detection of vertical ground movements by sea-level changes in the Neapolitan volcanoes. *Tectonophysics, 294*, 323–332. https://doi.org/10.1016/S0040-1951(98)00109-7

Biguino, B., Haigh, I. D., Antunes, C., Lamas, L., Tel, E., Dias, J. M., & Brito, A. C. (2024). Seasonal patterns, inter-annual variability, and long-term trends of mean sea level along the Western Iberian coast and the North Atlantic Islands. *Journal of Geophysical Research Oceans., 129*, 2023JC020742.

Blomfield, F. (1976). *Analysis of Time Series an introduction, 1st Editon*. Hoboken: Wiley.

Bult, S. V., Le Bars, D., Haigh, I. D., & Gerkema, T. (2024). The effect of the 18.6-year lunar nodal cycle on steric sea level changes. *Geophysical Research Letters*. https://doi.org/10.1029/2023GL106563

Carracedo, J. C., Singer, B., Jicha, B., Guillou, H., Rodríguez Badiola, E., Meco, J., Pérez Torrado, F. J., Gimeno, D., Socorro, S., & Láinez, A. (2003). La erupción y el tubo volcánico del Volcán Corona (Lanzarote, Islas Canarias). *Estudios Geológicos, 59*(5–6), 277–302. https://doi.org/10.3989/egeol.03595-6104

Carrère, L., Faugère, Y., & Ablain, M. (2016). Major improvement of altimetry sea level estimations using pressure-derived corrections based on ERA-Interim atmospheric reanalysis. *Ocean Science, 12*, 825–842. https://doi.org/10.5194/os-12-825-2016

Carrère, L., & Lyard, F. (2003). *Modeling the barotropic response of the global ocean to atmospheric wind and pressure forcing*. Comparisons with observations: Geophysical Research Letters. https://doi.org/10.1029/2002GL016473

Clette, F., Svalgaard, L., Vaquero, J. M., & Cliver, E. W. (2014). Revisiting the sunspot number. *Space Science Reviews, 186*, 35–103. https://doi.org/10.1007/s11214-014-0074-2

IERS Conventions. (2010). G. Petit & B. Luzum (Eds.). *IERS Technical Note* No. 36. https://www.iers.org/IERS/EN/Publications/TechnicalNotes/tn36.html

Cornish, C. R., Bretherton, C. S., & Percival, D. B. (2006). Maximal overlap wavelet statistical analysis with application to atmospheric turbulence. *Boundary-Layer Meteorology, 119*, 339–374. https://doi.org/10.1007/s10546-005-9011-y

Corrado, G., & Luongo, G. (1981). Ground deformation measurements in active volcanoes areas using tide gauges. *Bulletin of Volcanoly, 44*, 505–511. https://doi.org/10.1007/BF02600581

Ducarme, B., Venedikov, A. P., Arnoso, J., & Vieira, R. (2006). Analysis and prediction of ocean tides by the computer program VAV. *Journal of Geodynamics, 41*(1–3), 119–127.

Elneel, L., Zitouni, M. S., Mukhtar, H., & Al-Ahmad, H. (2024). Examining sea levels forecasting using autoregressive and prophet models. *Scientific Reports*. https://doi.org/10.1038/s41598-024-65184-0

Erol, S. (2011). Time-frequency analyses of tide-gauge sensor data. *Sensors, 11*(4), 3939–3961. https://doi.org/10.3390/s110403939

Fritier, N., Massei, N., Laignel, B., Durand, A., Dieppois, B., & Deloffre, J. (2012). Links between NAO fluctuations and interannual variability of winter months precipitation in the seine river watershed (north-western France). *Comptes Rendus. Géoscience, 344*, 396–405. https://doi.org/10.1016/j.crte.2012.07.004

García-Cañada, L. & Sevilla, M.J. (2005). Monitoring Crustal Movements and Sea Level in Lanzarote. *IAG Symposium*, Jaén, Spain, 17–19 March, 2005. https://hdl.handle.net/20.500.14352/53204.

García-Lafuente, J., Del Río, J., Álvarez-Fanjul, E., Gomis, D., & Delgado, J. (2004). Some aspects of the seasonal sea level variations around Spain. *Journal of Geophysical Research, 109*, C09008. https://doi.org/10.1029/2003JC002070

Gómez, M., Pérez-Gómez, B., De Alfonso, M., Pérez, S. & Ruiz, M. I. (2015). Waves and tides in the Canary Current Large Marine Ecosystem. In: *Oceanographic and biological features in the Canary Current Large Marine Ecosystem*. Valdés, L. and Déniz-González, I. (eds). IOC-UNESCO, Paris. IOC Technical Series, No. 115, pp. 115-131. URI: http://hdl.handle.net/1834/9182.

Grinsted, A., Moore, J. C., & Jevrejeva, S. (2004). Application of the cross-wavelet transform and wavelet coherence to geophysical time series. *Nonlinear Processes in Geophysics, 11*(56), 561–566.

Online document Met Office, Hadley Centre, HadISST 1.1. (2006). Global sea-Ice coverage and SST (1870-Present). NCAS British Atmospheric Data Centre. Retrieved May, 2024, from https://www.metoffice.gov.uk/hadobs/hadisst/index.html

Hernández, A., Martin-Puertas, C., Moffa-Sánchez, P., Moreno-Chamarro, E., Ortega, P., Blockley, S., Cobb, K. M., Comas-Bru, L., Giralt, S., Goosse, H., Luterbacher, J., Martrat, B., Muscheler, R., Parnell, A., Pla-Rabes, S., Sjolte, J., Scaife, A. A., Swingedouw, D., Wise, E., & Xu, G. (2020). Modes of climate variability: Synthesis and review of proxy-based reconstructions through the Holocene. *Earth-Science Reviews*. https://doi.org/10.1016/j.earscirev.2020.103286

Hwang, C., Yang, Y., Kao, R., Han, J., Shum, C. K., Galloway, D. L., Sneed, M., Hung, W. C., Cheng, Y., & Li, F. (2016). Time-varying land subsidence detected by radar altimetry: California. *Taiwan and North China. Scientific Reports, 6*, 28160. https://doi.org/10.1038/srep28160

Kirikkaleli, D., & Sowah, J. K. (2021). Time-frequency dependency of temperature and sea level: A global perspective. *Environment Science Pollution Research, 28*, 58787–58798. https://doi.org/10.1007/s11356-021-14846-x

Le Mouël, J. L., Lopes, F., & Courtillot, V. (2020). Characteristic time scales of decadal to centennial changes in global surface temperatures over the past 150 years. *Earth and Space Science*. https://doi.org/10.1029/2019EA000671

Li, Q. (2008). Periodicity and hemispheric phase relationship in high-latitude solar activity. *Solar Physics, 249*, 135–145.

Lombard, A., Cazenave, A., Le Traon, P. Y., & Ishii, M. (2005). Contribution of thermal expansion to present-day sea-level change revisited. *Global and Planetary Change, 47*, 1–16.

Marrero-Betancort, N., Marcello, J., Rodríguez-Esparragón, D., & Hernández-León, S. (2022). Sea level change in the canary current system during the satellite era. *Journal of Marine Science and Engineering, 10*, 936. https://doi.org/10.3390/jmse10070936

Martinez García, A., Gonzalez, B. C., Núñez, J., Wilkens, H., Oromí, P., Íliffe, T. M., & Worsaae, K. (2016). *Guide to the anchialine ecosystems of Los Jameos del Agua and Túnel de la Atlántida*. Cabildo de Lanzarote. ISBN-13: 978-84-95938-92-3.

Menemenlis, D., Campin, J., Heimbach, P., Hill, C., Lee, T., Nguyen, A., Schodlok, M., & Zhang, H. (2008). ECCO2: High resolution global ocean and sea ice data synthesis. *Mercator Ocean Quartely Newsletters, 31*, 13–21.

Oelsmann, J., Marcos, M., Passaro, M., Sanchez, L., Dettmering, D., Dangendorf, S., & Seitz, F. (2024). Regional variations in relative sea-level changes influenced by nonlinear vertical land motion. *Nature Geoscience, 17*, 137–144. https://doi.org/10.1038/s41561-023-01357-2

Percival, D. B., & Mofjeld, H. O. (1997). Analysis of subtidal coastal sea level fluctuations using wavelets. *Journal of the American Statistical Association, 92*(439), 868–880. https://doi.org/10.1080/01621459.1997.10474042

Percival, D. B., & Walden, A. T. (2000). *Wavelet methods for time series analysis* (p. 594). London: Cambridge University Press.

Pugh, D., & Woodworth, P. L. (2014). *Sea-level science: Understanding tides, surges, tsunamis and mean sea-level changes*. Cambridge University Press. https://doi.org/10.1017/CBO9781139235778

Rayner, N. A., Parker, D. E., Horton, E. B., Folland, C. K., Alexander, L. V., Rowell, D. P., Kent, E. C., & Kaplan, A. (2003). Global analyses of sea surface temperature, sea ice, and night marine air temperature since the late nineteenth century. *Journal If Geophysical Reseach, 108*(D14), 4407. https://doi.org/10.1029/2002JD002670

Riccardi, U., Arnoso, J., Benavent, M., Vélez, E., Tammaro, U., & Montesinos, F. G. (2018). Exploring deformation scenarios in Timanfaya volcanic area (Lanzarote, Canary Islands) from GNSS and ground based geodetic observations. *Journal of*

Volcanology and Geothermal Research, 357, 14–24. https://doi.org/10.1016/j.jvolgeores.2018.04.009

Rizvi, S. H. M., Abbas, M., Zaidi, S. S. H., Tayyab, M., & Malik, A. (2024). LSTM-based autoencoder with maximal overlap discrete wavelet transforms using lamb wave for anomaly detection. *Composites. Applied Sciences, 14*, 2925. https://doi.org/10.3390/app14072925

Siemer, J. P., Machín, F., GonzálezVega, A., Arrieta, J. M., GutiérrezGuerra, M. A., Pérez-Hernández, M. D., et al. (2021). Recent trends in SST, Chl-a, productivity and wind stress in upwelling and open ocean areas in the upper Eastern North Atlantic subtropical gyre. *Journal of Geophysical Research: Oceans.* https://doi.org/10.1029/2021JC017268

Song, C., Chen, X., & Xia, W. (2023). Improving the understanding of the influencing factors on sea level based on wavelet coherence and partial wavelet coherence. *Journal of Oceanology and Limnolology, 41*, 1643–1659. https://doi.org/10.1007/s00343-022-2102-5

Tammaro, U., Obrizzo, F., Riccardi, U., La Rocca, A., Pinto, S., Brandi, G., & Capuano, P. (2021). Neapolitan volcanic area Tide Gauge Network (Southern Italy): Ground displacements and sea-level oscillations. *Advances in Geosciences, 52*, 105–118.

The MathWorks Inc. (2023). MATLAB version: R2023b, Natick, Massachusetts: The MathWorks Inc. https://www.mathworks.com

Torrence, C., & Compo, G. P. (1998). A practical guide to wavelet analysis. *Bulletin of the American Meteorology Society, 79*, 61–78.

Torrence, C., & Webster, P. J. (1999). Interdecadal changes in the ENSO-Monsson System. *Journal of Climate, 12*, 2679–2690.

Tsimplis, M. N., Calafat, F. M., Marcos, M., Jordà, G., Gomis, D., Fenoglio-Marc, L., Struglia, M. V., Josey, S. A., & Chambers, D. P. (2013). The effect of the NAO on sea level and on mass changes in the Mediterranean Sea. *Journal of Geophysical Research Oceans, 118*(2), 944–952. https://doi.org/10.1002/jgrc.20078

van Dam, T. M., Wahr, J., Chao, Y., & Leuliette, E. (1997). Predictions of crustal deformation and of geoid and sea-level variability caused by oceanic and atmospheric loading. *Geophysical Journal International, 129*, 507–517. https://doi.org/10.1111/j.1365-246X.1997.tb04490.x

Vargas-Yáñez, M., Tel, E., Marcos, M., Moya, F., Ballesteros, E., Alonso, C., & García-Martínez, M. C. (2023). Factors contributing to the long-term sea level trends in the iberian peninsula and the balearic and canary Islands. *Geosciences, 13*, 160.

Venedikov, A. P., Arnoso, J., Cai, W., Vieira, R., Tan, S., & Velez, E. J. (2006). Separation of the long-term thermal effects from the strain measurements in the geodynamics laboratory of lanzarote. *Journal of Geodynamics*. https://doi.org/10.1016/j.jog.2005.08.029

Venedikov, A., Arnoso, J., & Vieira, R. (2003). VAV: A program for tidal data processing. *Computer & Geosciences, 29*(4), 487–502. https://doi.org/10.1016/S0098-3004(03)00019-0

Venedikov, A., Arnoso, J., & Vieira, R. (2005). New version of program VAV for tidal data processing. *Computer & Geosciences, 31*(5), 667–669. https://doi.org/10.1016/j.cageo.2004.12.001

Veronig, A. M., Jain, S., Podladchikova, T., Pötzi, W., & Clette, F. (2021). Hemispheric sunspot numbers 1874–2020. *Astronomy & Astrophysics, 652*, A56. https://doi.org/10.1051/0004-6361/202141195

Vieira, R., Van Ruymbeke, M., Fernandez, J., Arnoso, J., & Toro, C. (1991). The lanzarote underground laboratory. *Cahiers Du Centre Europeén De Géodynamique Et De Seîsmologie, 4*, 71–86.

Whitcher, B., Guttorp, P., & Percival, D. B. (2000). Wavelet analysis of covariance with application to atmospheric time series. *Journal of Geophysical Research: Atmospheres, 105*(D11), 14941–14962.

Williams, S. D. P., & Penna, N. T. (2011). Non-tidal ocean loading effects on geodetic GPS heights. *Geophysical Research Letters*. https://doi.org/10.1029/2011GL046940

Wöppelmann, G., & Marcos, M. (2016). Vertical land motion as a key to understanding sea level change and variability. *Reviews of Geophysics,54*(1), 64–92. https://doi.org/10.1002/2015RG000502

Yamakawa, S., Inoue, M., & Suppiah, R. (2016). Relationships between solar activity and variations in SST and atmospheric circulation in the stratosphere and troposphere. *Quaternary International, 397*, 289–299. https://doi.org/10.1016/j.quaint.2015.11.018

Zerbini, S., Matonti, F., Raicich, F., & Van Dam, T. (2004). Observing and assessing nontidal ocean loading using ocean, continuous GPS and gravity data in the Adriatic area. *Geophysical Research Letters*. https://doi.org/10.1029/2004GL021185

Zhu, Y., Han, W., & Alexander, M. A. (2023). Nonstationary roles of regional forcings in driving low-frequency sea level variability along the US east coast since the 1950s. *Geophysical Research Letters*. https://doi.org/10.1029/2023GL104191

(Received June 27, 2024, revised November 27, 2024, accepted December 12, 2024)